The Pennsylvania State University

The Graduate School

Department of Energy and Mineral Engineering

PARAMETRIC STUDY OF FACTORS AFFECTING

CAPILLARY IMBIBITION IN FRACTURED POROUS MEDIA

A Dissertation in

Petroleum and Mineral Engineering

by

Chung-Hao Lee

Submitted in Partial Fulfillment
of the Requirements
for the Degree of

Doctor of Philosophy

May 2011

The dissertation of Chung-Hao Lee was reviewed and approved* by the following:

Zuleima T. Karpyn
Assistant Professor of Petroleum and Natural Gas Engineering
Quentin E. and Louise L. Wood Faculty Fellow in Petroleum and Natural Gas
Engineering
Dissertation Advisor
Chair of Committee

Yaw D. Yeboah
Professor and Department Head of Energy and Mineral Engineering

Turgay Ertekin
Professor of Petroleum and Natural Gas Engineering
George E. Trimble Chair in Earth and Mineral Sciences

Derek Elsworth
Professor of Energy and Geo-Environmental Engineering

John Yilin Wang
Assistant Professor of Petroleum and Natural Gas Engineering

Kamini Singha
Assistant Professor of Geosciences

*Signatures are on file in the Graduate School

ABSTRACT

Capillarity, gravity and viscous forces control the fluids migration in geologic formations. However, experimental working addressing the simultaneous action of these driving forces as well as the impact of injection flow rate in fractured porous media is limited. Understanding how these variables affect fracture-matrix transfer mechanisms and invasion front evolution in fractured rocks are of crucial importance to modeling and prediction of multiphase ground flow. This study addresses the simultaneous influence of fracture orientation, rock and fluid properties, and flowing conditions on multiphase flow in fractured permeable media at laboratory scale. Displacement of a non-wetting phase (gas or liquid) by capillary imbibition was monitored using X-ray computed tomography (CT). Results were then mimicked using an automated history matching approach to obtain representative relative permeability and capillary pressure curves to further investigate the impact of matrix homogeneity/heterogeneity and boundary shape on the response of the imbibition front. Sensitive analyses, in combination with direct experimental observation, allowed us to explore relative importance of relative permeability and capillary pressure curves to saturation distribution and imbibing font evolution.

Experimental observations combined with simulation results indicated the impact of fracture orientation on imbibition front evolution was minimal for the time- and length-scales considered in this investigation. While different injection rates and fluid types showed significant differences in the shape of the imbibing front, breakthrough time, and saturation profiles. The speed and shape of imbibing front progressions were found to be sensitive to matrix water relative permeability, capillary pressure contrast between matrix and fracture, and degree of rock heterogeneity. Results from this work also demonstrated conditions that favor co-current, counter-current, and the coexistence of both displacement mechanisms during imbibition. Co-current flow dominates in the case of water displacing air, while counter-current flow dominates in the case of water displacing

kerosene. The balance of capillarity and relative permeabilities has a significant impact of the shape on the invasion front, resulting in periods of co-current and counter-current imbibition. This work presents direct evidence of spontaneous migration of wetting fluids into a rock matrix embedding a fracture. These observations and conclusions are not limited by the geometry of the system and have important implication for water flooding of naturally fractured reservoir and leak-off retention and migration after hydraulic fracture treatments.

TABLE OF CONTENTS

vii

LIST OF FIGURES

Pages

LIST OF TABLES

Pages

ACKNOWLEDGEMENTS

Chapter 1

Introduction

Fractures serve as primary conduits having great impact on the migration of injected fluid into fractured permeable media. This research study is a multi-variable analysis of fracture-matrix flow including the effects of injection flow rate, fluid type, fracture orientation and flow direction. In the first section of this study (see Chapter 2), we analyze the impact of two different injection rates on the capillary dominated displacement of oil by water in fractured rock samples, using x-ray computed tomography. A laboratory flow apparatus was designed specifically for this set of experiment, in which saturation maps are monitored as a function of time for two injection flow rates. X-ray computed tomography (CT) was used to record these saturation maps as a function of time. Continuous CT scanning allowed us to track capillary imbibition into a fractured Berea sandstone sample originally saturated with kerosene.

Experiments were later extended to cover different fluid types and five different fracture configurations with flow directions (see Chapter 3). This experimental investigation addresses the influence of viscosity ratio and fracture orientation on the progression of an imbibition front in fractured permeable media at laboratory scale. Three different fluid pairs including air-brine, kerosene-brine and a viscous oil-brine, and five different fracture configurations were investigated to address the influence of viscosity ratio and fracture orientation on oil recovery and saturation maps. Experimental results of two-phase (kerosene-brine) floods are then mimicked using an automated history matching approach to obtain representative matrix and fracture relative permeability and capillary pressure curves (see Chapter 4). These curves were then used to predict imbibition front evolution under different flow conditions, which result in excellent agreement with

experimental observations. Sensitivity analyses and predictive simulation tests were provided to further investigate the effects of transport properties and shapes of boundary on oil displacement and imbibition front evolution. Results from this investigation provide a comprehensive set of data for the validation of numerical models and strengthen fundamental understanding of multiphase flow in fractured rocks.

Chapter 2

Experimental Investigation of Rate Effects

Understanding how injection flow rate affects fracture-matrix transfer mechanisms and invasion front evolution in fractured reservoirs are of crucial importance to modeling and prediction of multiphase ground flow. However, experimental work addressing the impact of injection flow rate in fractured core samples is limited. In this chapter, we monitor and analyze transfer mechanisms in fractured rock samples using medical X-ray computed tomography. The impact of different injection rates on the resulting fluid recovery and saturation maps is evaluated through visual and quantitative analyses. Results from this work help visualize the impact of injection flow rate on the dynamics of fracture-matrix transport and, at the same time, provide detailed quantitative information for the validation of representative numerical models of fractured permeable reservoirs.

2.1 Literature Review

Fluid displacement in fractured media is of interest for many environmental and engineering processes. Examples include CO_2 geological sequestration, nuclear waste disposal, geothermal power generation, and enhanced oil recovery in natural fracture reservoir (Berkowitz (2002); Committee on Fracture Characterization and Fluid Flow (1996)). The presence of fractures not only provide preferential pathways for fluid migration, but also gives rise to a range of complex flow phenomena. Crandall et al. (2010) conducted a series of simulations for flows in fractured permeable rocks, and observed more than 5% increase in the volumetric flow rate within high permeability-fractured porous media. Karpyn et al. (2009) found that bedding planes adjacent to fracture zones with higher aperture tend to have higher porosity, and higher permeability, thus affecting the overall hydraulic conductivity of the system. This higher hydraulic conductivity leads to higher flow rate in the fracture zone and makes injected fluids easily

breakthrough and low efficiency displacement in the porous matrix. Alajmi and Grader (2000) used x-ray CT to study two-phase flow displacements in layered Berea samples with fracture tips. The results showed the presence of the fracture significantly delayed the oil recovery. In addition, different flow behaviors, co-current and counter-current imbibition were observed at three different regions in the sample, the fracture region, the non-fractured region, and the fracture tip. Rangel-German and Kovscek (2002) used x-ray CT to study capillary imbibition of air and oil displacement by water from rock samples. They identified two different fracture flow regimes, co-current and counter-current imbibition. Counter-current imbibition is occurring when the fractures refills with water at a faster rate than it can be transferred through the fracture-matrix interface, while co-current shows when relatively slow flow through fractures.

Different flow regimes were observed at different injection flow rate. Melean et al. (2003) conducted a series of imbibition experiments in porous medium at different injection rates by using CT scan measurements. The results showed the water front spread smoothly and increased evenly at low rates, while the water front spread rapidly and inclined to the outlet at high rate cases. Babadagli (1994) found that as the injection rate is increased, fracture pattern becomes an important parameter controlling the saturation distribution in the rock matrix. As the rate is lowered, however, the system begins to behave like a homogeneous system showing a frontal displacement regardless of the fracture configuration. Similar observation can be obtained from Babadagli (2000). Although these, and other studies (Prodanovic et al. (2008), Hoteit and Firoozabadi (2008), Donato et al. (2007), and Rangel-German et al. (2006)) have contributed to current understanding of multiphase flow in fractured systems, there is still limited understanding of the relative impact of injection rate affecting two-phase displacement mechanisms in fractured rocks. Analyzing how injection rate affects fracture-matrix flow, especially under capillary dominated conditions, remains largely unexplored and it is the main goal of this section.

2.2 Experiment Design

The purpose of this design was to create a two-dimensional flow system within a sample holder, to allow complete sample monitoring with a single-slice CT scanning as shown in Figure 2-1. By making the sample a thin disk, we eliminate one flow direction, the one orthogonal to the disk. Therefore, a single slice is sufficient to capture the entire fracture and the surrounding rock matrix, thereby allowing us to keep track of saturation changes at small time intervals. The rock sample used in this study was Berea Sandstone. Each sample disk has a diameter of 102 mm and thickness of 10 mm. A single tensile fracture was created artificially on each disk. All fractures are aligned with the centre of the sample and perpendicular to the bedding layers. Fracture apertures are around 0.5mm. Pore volume of the matrix and fracture are 18.51mL and 0.51mL, respectively. The experimental apparatus includes three major portions: sample holder, fluid supply system and X-ray CT scanner.
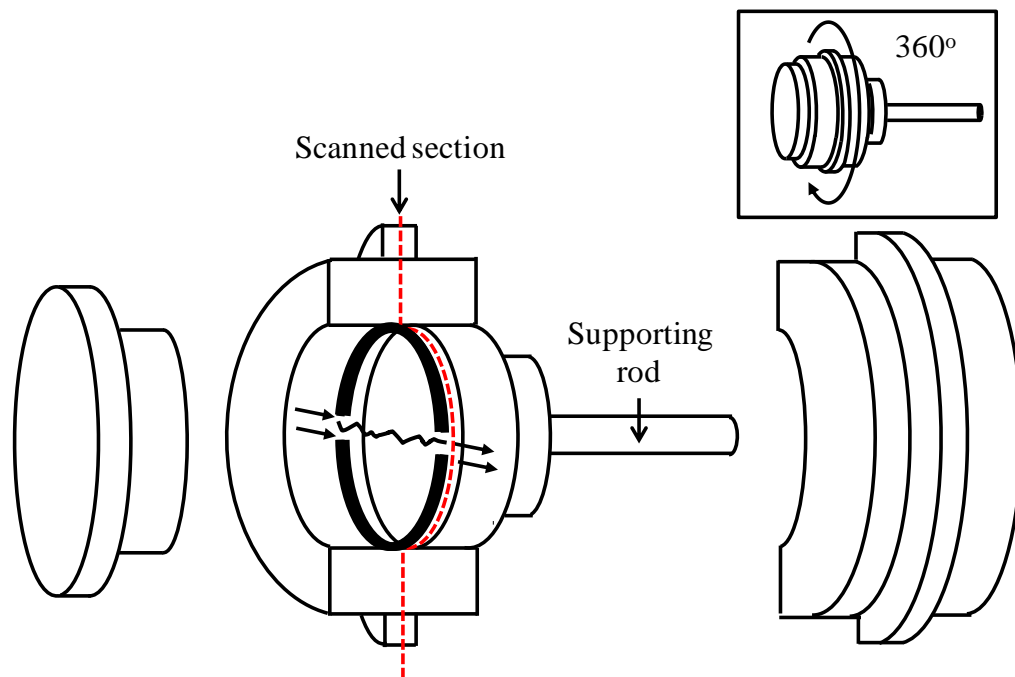
Figure 2-1: Schematic drawing of experimental design.

2.2.1   Sample Holder

A cake-shaped sample holder was fabricated according to the diagram shown in Figure 2-2 and Figure 2-3. After assembling pieces A, B and inserting piece C, a trapped volume is obtained with a diameter of 104 mm and a thickness of 10 mm. This sample holder is made of Teflon to avoid chemical reaction with fluids, and only Teflon and the rock sample are intercepted by the scanning plane. Viton rubber sheets are used to seal the gap between the sample and the walls of the holder, thus blocking potential pathways around the sample and allowing fluid flow through the fracture alone. The supporting rod, also shown in the top-right insert in Figure 2-1, can rotate in 45 degree increments, and it is attached in such a way that the cell can rotate on its horizontal axis. Although the core holder is designed to allow different fracture inclinations and flow directions with this rotation system, this section focuses on experiments using a horizontal fracture. A similar rotation system was used in a core holder designed for gravity segregation experiments by Karpyn et al. (2006). Figure 2-4 (left) shows a sample disk with fracture perpendicular to the bedding layers and Figure 2-4 (right) shows a photograph of all the pieces forming the core holder.
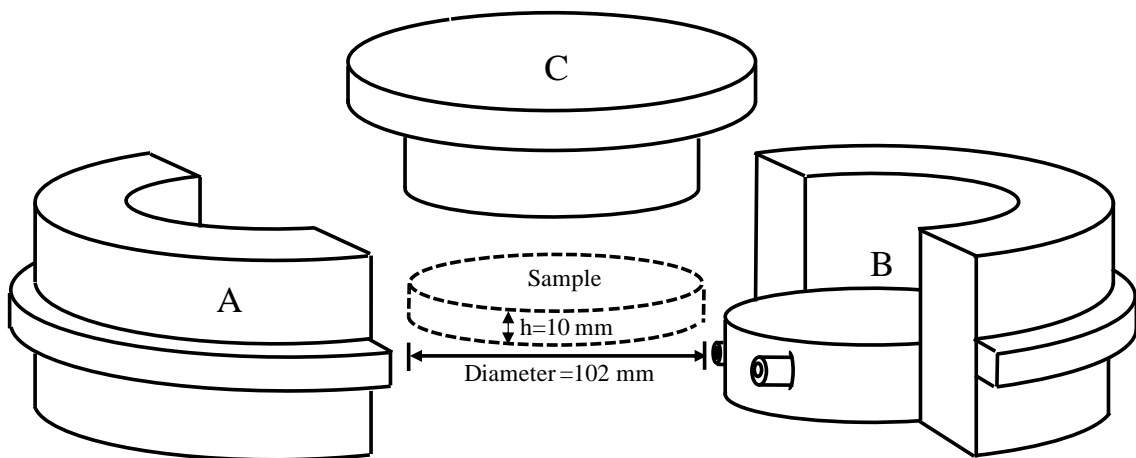
Figure 2-2: Schematic drawing of sample holder design.
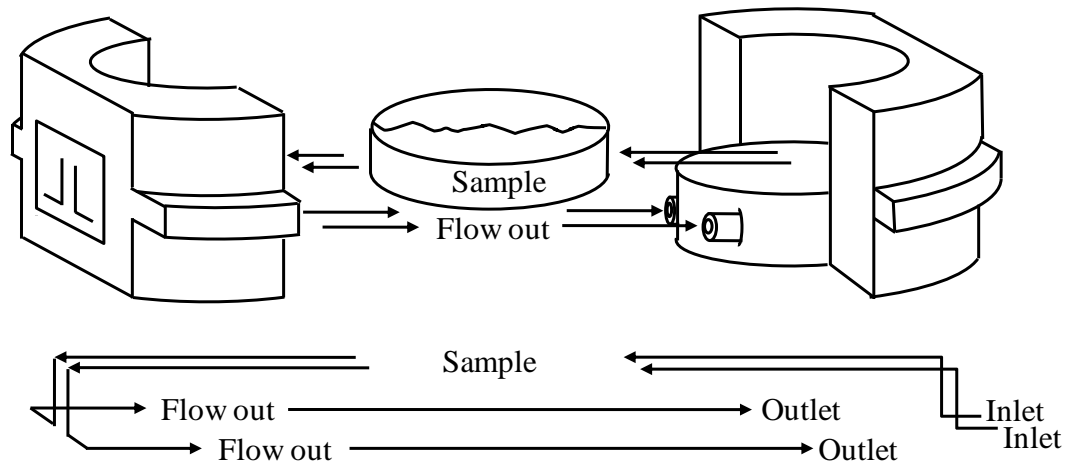
Figure 2-3: Schematic drawing of flow pathway within sample holder.
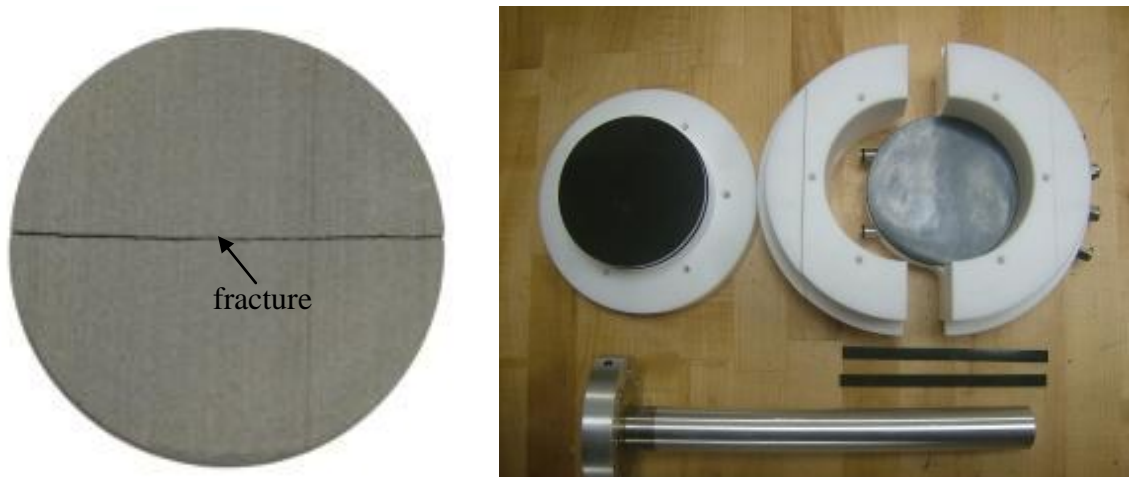
Figure 2-4: A sample disk with fracture perpendicular to the bedding layers (left), and Teflon core holder, Viton rubber sheets (black) and support rod (right).

2.2.2 X-ray CT scanner

Fluid saturation distributions are computed using X-ray computed tomography (CT) scanning. X-Ray CT is a non-destructive imaging technique that uses X-rays and mathematical reconstruction algorithms to view the internal properties of an object (Vinegar and Wellington (1987)). It is also used to quantify rock heterogeneities, determine lithologies and porosities, and monitor fluid saturations during flow processes. A medical HD350 scanner with a detection limit of 25 microns was used in this study. The CT system consists of an ionized X-Ray source, a detector, a translation system, and a computer system that controls motions and data acquisition. Each CT image produces a matrix of 512 by 512 pixels covering the entire sample. The voxel size selected to this work was $5.00\times0.205\times0.205$ mm. Figure 2-5 shows the schematic drawing of medical CT scanner used in this study, which locates in the Center for Quantitative X-Ray Imaging (CQI) at Penn State University.
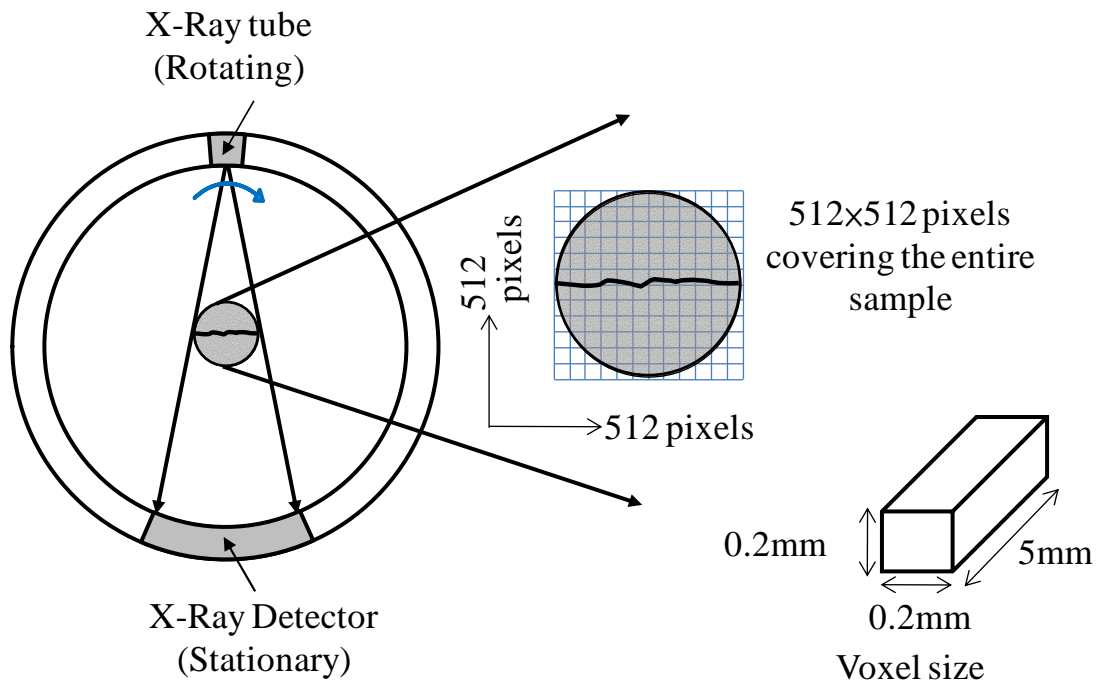
Figure 2-5: Schematic drawing of X-Ray CT Scanner.

2.2.3   Fluid Circulation System

The fluids used in the present experiments are distilled water and kerosene. Distilled water was tagged with 15% by weight of sodium iodide (NaI) to increase its CT registration and provide a high contrast between the two phases. The viscosity of tagged water is approximately 1.80 cP (centipoise) and that for kerosene is 4.06cP. The physical properties of these fluids are shown in Table 2-1. Before commencing the experiment, two immiscible fluids, oil and water phases, were thoroughly mixed with each other and allowed to separate under gravity action. This procedure minimizes in-situ changes in saturation due to mutual solubility.

A schematic representation of this system is presented in Figure 2-6. A vacuum pump enables the sample holder reach 250 microns vacuum condition. This vacuum state is used to pre-saturate the sample with oil phases. A syringe pump (LC-5000) delivers tagged water (brine) into the sample through the fracture. To guarantee a predominantly capillary-driven displacement, injection flow rates are low, in the order of 40mL/hr and 4mL/hr, which correspond to capillary numbers in the order of 4.8×10^{-4} and 4.8×10^{-5}, respectively. The capillary number represents the relative control of viscous force over capillary force. For capillary numbers below 10^{-5}, flow in porous media is considered to be dominated by capillary forces (Ding and Kantzas (2007)). The equation for calculating the capillary number is

$$N_{ca} = \frac{\mu \cdot v}{\gamma}$$ ....[2-1]

where μ is the viscosity of the liquid, v is a characteristic velocity and γ is the surface or interfacial tension between the two fluid phases.
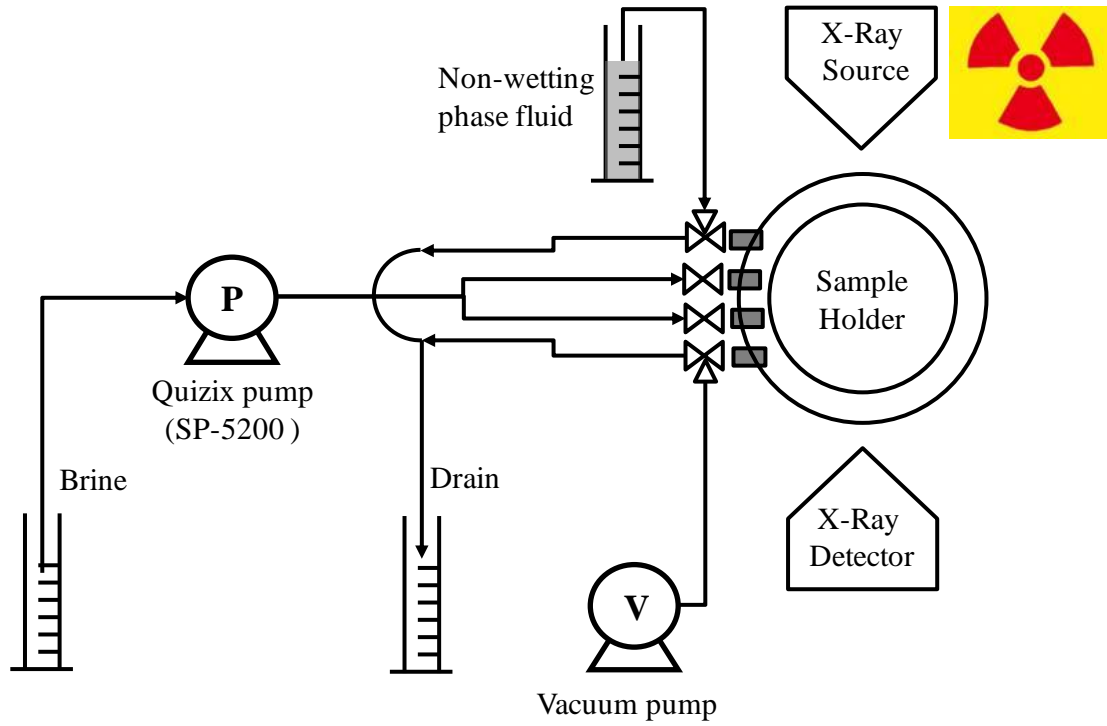
Figure 2-6: Schematic drawing of fluid circulation system.

Table 2-1: Physical properties of fluids.

Phases	Fluid composition	Viscosity at 25.7°C (cP)	Specific gravity at 25.7°C
Water	Tagged water (15% NaI by weight)	1.0	1.0
Oil	Kerosene	2.9	0.79

2.3 Experimental Procedure

A schematic representation of the experimental procedure is presented in Figure 2-7. The dry fractured sample was mounted and vacuumed in the sample holder and scanned to observe its heterogeneity and its layered structure (stage 1 in Figure 2-7). In stage 2, the sample was pre-saturated with oil (non-wetting phase) and scanned. The image difference between these two stages is used for porosity calculations. In stages 3 and 4, the sample was flooded by injecting water. Fluid saturations were continuously monitored by scanning at specific time intervals until residual oil saturation was reached. At the same time, oil recovery is recorded as a function of time at the outlet.

1. Vacuum sample and scan	2. Saturate sample and scan	3. Begin water injection	4. End of water injection
Scan dry slice for fracture identification and rock heterogeneities	Scan slice filled with non-wetting phase. This will be a reference state	Start continuous scanning of slice during water injection	Continue Scanning during water injection
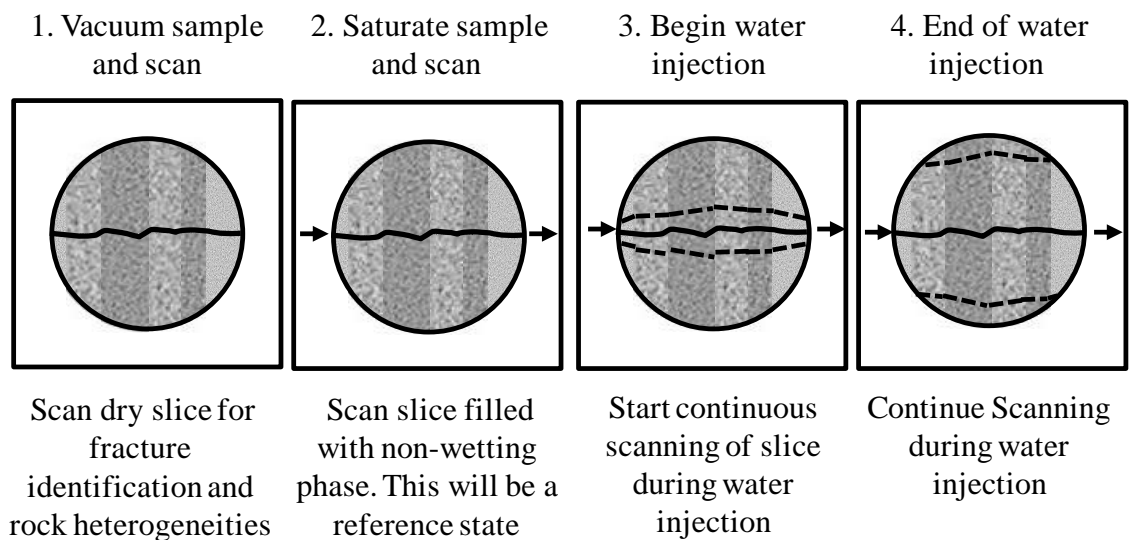
Figure 2-7: Experimental procedure and CT scanning sequence for oil-water system.

2.4 Determination of Porosity and Fluid Saturation

The average sample porosity (ϕ_{avg}) is 23.27% obtained from the volume of oil used in saturating the sample and the bulk volume of the sample. Pixel porosities (ϕ_{pixel}) were obtained from Equation [2-2] using X-ray CT registrations from the vacuum condition in stage 1(CT_{vacuum}) and the oil saturated condition in stage 2 (CT_{sat}) as shown in Figure 2-7.

$$\phi_{pixel} = \frac{CT_{sat} - CT_{vacuum}}{\left(CT_{sat} - CT_{vacuum}\right)_{avg}} \phi_{avg} \dots\dots\dots\dots\dots\dots\dots\dots\dots\dots\dots\dots\dots\dots\dots\dots.[2\text{-}2]$$

In situ saturations were also determined using data from the CT scanner. Pixel water saturations ($S_{w,pixel}$) were obtained from Equation [2-3], where ϕ_{pixel} is the pixel porosity from Equation [2-2], $S_{w,avg}$ is the average saturation of water in the sample obtained from the linear correlation between 100% water saturated ($CT_{w,avg}$) and 100% oil saturated sample ($CT_{sat,avg}$).

$$S_{w,pixel} = \frac{CT_{sat} - CT_f}{\left(CT_{sat} - CT_f\right)_{avg}} \cdot \left(\frac{\phi_{avg}}{\phi_{pixel}}\right) \cdot S_{w,avg} \dots\dots\dots\dots\dots\dots\dots\dots\dots\dots\dots\dots\dots \ [2\text{-}3]$$

$$S_{w,avg} = \frac{CT_{f,avg} - CT_{sat,avg}}{CT_{w,avg} - CT_{sat,avg}} \dots\dots\dots\dots\dots\dots\dots\dots\dots\dots\dots\dots\dots\dots.[2\text{-}4]$$

2.5 Results and Discussion

In this section, we compare two different injection flow rates using the same fluid type, kerosene and brine. Average saturation changes as a function of time and pore volume injected are presented in Figure 2-8. These saturations were averaged over the entire sample, including fracture and rock matrix. In Figure 2-8 top, water breakthrough for the low-rate curve in red is delayed 10 min with respect to the high-rate blue curve. In addition, the high-rate curve (q=40mL/hr) reaches higher water saturation, and thus higher oil recovery, sooner than the low-rate case, but it requires more pore volume

injected to reach that saturation level, as seen in Figure 2-8 bottom. After approximately 300 minutes of water injection, oil recovery becomes negligible in both cases, when water saturation reaches 0.56. Under this final saturation conditions, both oil and water are still mobile inside the rock sample, but the increments in water saturation are too small to be appreciated in the lapse of a few days.

Figure 2-9 are time progressions of water saturation (Sw) maps corresponding to high and low water injection rate. Dark blue represents regions saturated with kerosene (Sw=0.0), red represents regions saturated with water (Sw=1.0), and intermediate colors represent the co-existence of kerosene and water in the pore space. For the high-rate case (Figure 2-9 top) we see a sharp increase in water saturation in the neighborhood of the fracture, and a maximum in the fracture itself and the outlet (right end of the fracture). Under these flowing conditions, the fractures refills with water at a faster rate than it can be transferred through the fracture-matrix interface, confirming similar experimental observations found in the literature (Rangel-German and Kovscek (2006)). Simultaneously, counter-current imbibition is occurring in the water invaded zone as oil is expelled from the matrix into the fracture. As time progresses, the imbibition front moves away from the fracture, and water accumulation becomes evident around the outlet end of the fracture (right side) in red, supporting the fact that the rate of capillary dispersion through the matrix is low compared to the rate of injection. The rate of injection is also responsible for the shape of the imbibing front, which is farther away from the fracture inlet than the outlet. These mechanistic observations are less pronounced when the rate of injection is reducing.

Figure 2-9 bottom shows an analogous progression of water saturation maps obtained at 4mL/hr of water injection. The contrast in saturation ahead and behind the water front is not as sharp as that in Figure 2-9 top. This is evident in a smoother color transition, passing from dark to light blue, to green, and finally yellow and red.
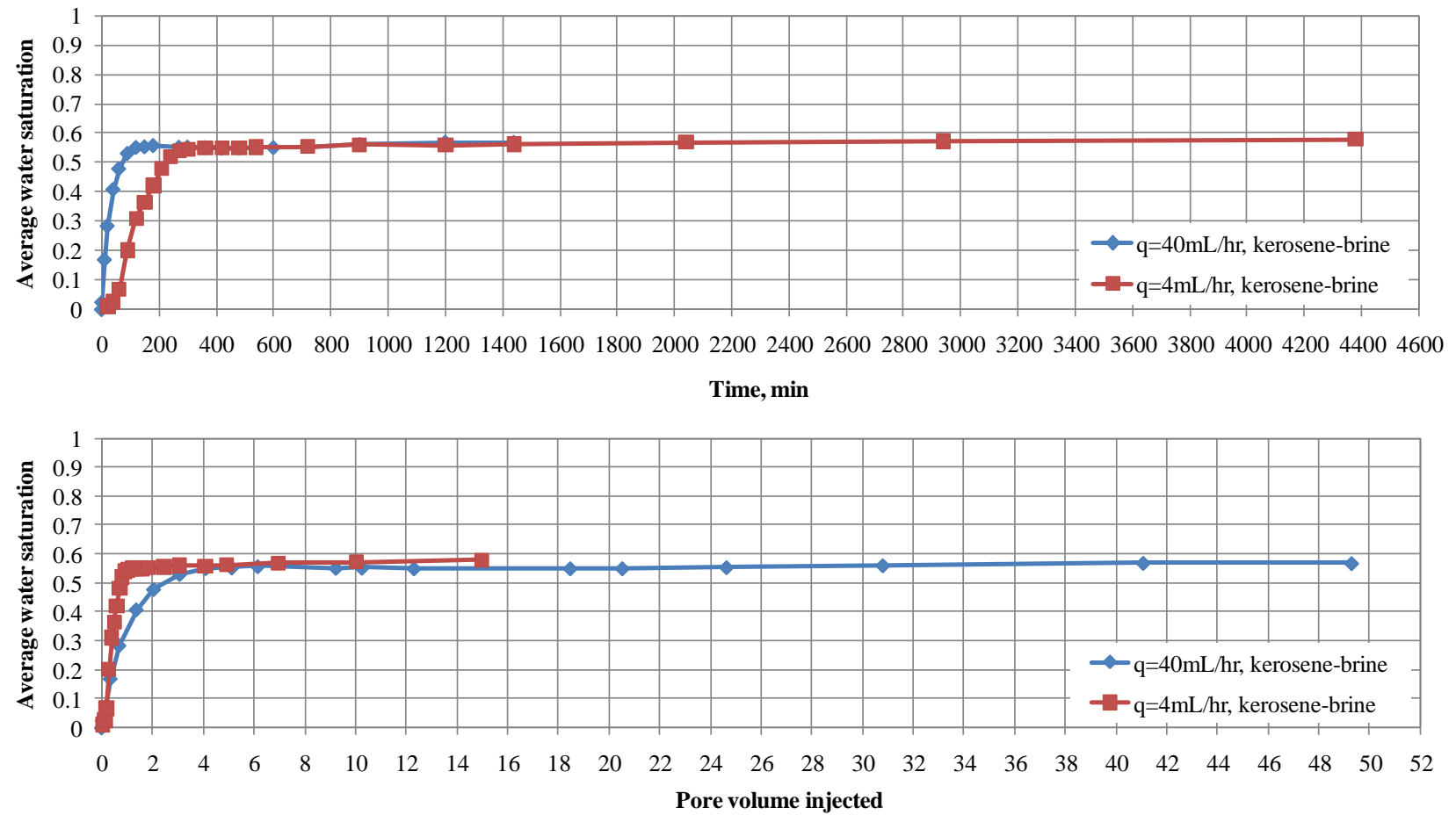
Figure 2-8: Average water saturation as a function of time, showing the effect of injection rate.
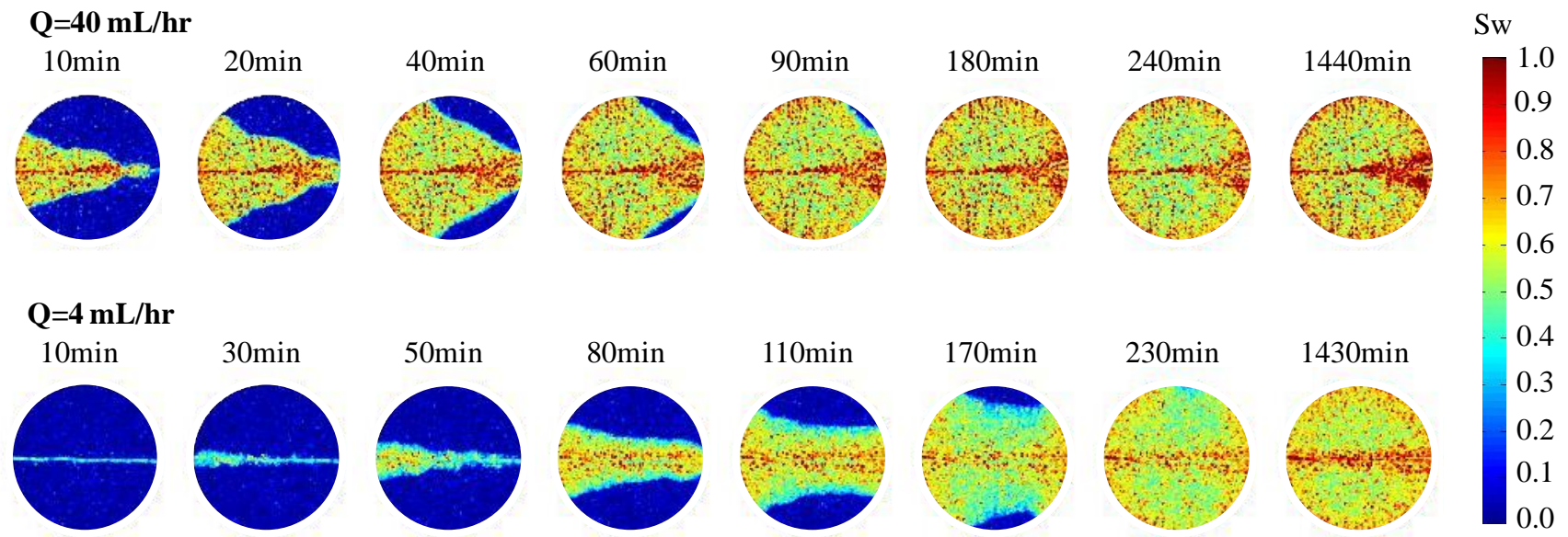
Figure 2-9: Time progression of water saturation maps corresponding to 40mL/hr (top) and 4mL/hr (bottom) brine injection rate, kerosene-brine experiment.

In addition, for the same pore volume injected, that is 0.7 PVI at 20 min high-rate (40mL/hr) and 170 min low-rate (4mL/hr), we observe a much larger imbibed region in the low-rate case, implying low injection rate allows a more effective spreading of water for the same volume injected. At the late time (t=1440), water collects around the fracture's outlet end. This is depicted by the red cone shape observed at the right side of the sample.

Further quantitative examination of saturation changes obtained from CT scanning is presented in Figure 2-10. These vertical saturation profiles averaged over the central 6 mm of each CT slice for the two flow rates under study. These profiles capture saturation changes with time in the direction perpendicular to the fracture. For both experiments, continuous high water saturation is observed in the center of the sample, where the fracture is located. The most salient differences between these two groups of vertical profiles are: (1) the speed at which the water front moves away from the fracture, which was also evident in the saturation maps, presented in Figure 2-9; and (2) the change in saturation as we move away from the fracture. Figure 2-10 right shows a gradual saturation change at the front, while there is a drastic drop in saturation across the water front in Figure 2-10 left. Furthermore, water saturations remain in the 0.50-to-0.55 range within the imbibed zone, which suggests that both fluid phases are under a dynamic equilibrium at that saturation. This is consistent with the knowledge that counter-current flow is the prevalent flow mechanism in the imbibed zone. As the water front progresses, the resident oil is displaced towards the fracture, in a counter-current manner, and replenished by the oil that is sitting ahead of the front, thus maintaining a dynamic equilibrium and a constant saturation in the imbibed zone.
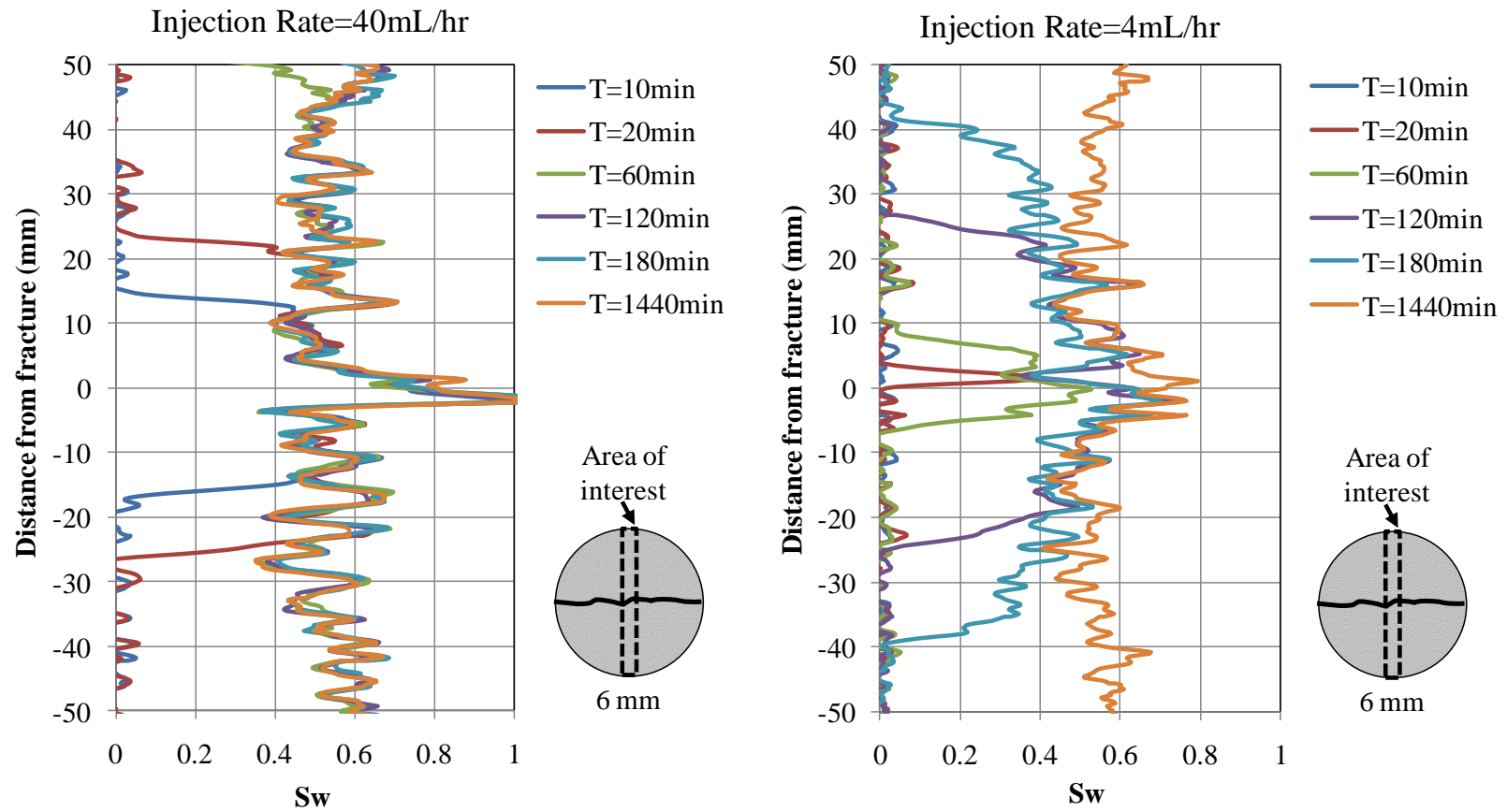
Figure 2-10: Vertical saturation profiles perpendicular to the fracture and averaged over the central 6 mm of the sample, Kerosene-brine experiment, q=40mL/hr (left) and q=4mL/hr (right).

Chapter 3

Impact of Viscosity Ratio and Fracture Orientation

The objective of this section is to investigate the effects of viscosity ratio and fracture orientation on oil recovery and water front evolution using medical X-Ray computed tomography (CT). First, we compare three different fluid pairs with different viscosity ratio in horizontal fractured rock samples. These experiments were then extended to include five different fracture configurations in the case of water displacing air to evaluate the impact of fracture orientations. A detailed delineation of the impact of viscosity ratio as well as fracture orientation on the dynamics of fracture-matrix transport is presented and provides reference background to qualify the migration and trapping of leak-off fracturing fluids in hydraulic fracture under shut-in conditions.

3.1   Literature Review

In general, capillarity, gravity and viscous force are three major driving forces control fluids migration in geological formations. Numerous studies had demonstrated the importance of these forces whether from experiments (Lefebvre du prey (1978), Ovdat and Berkowitz (2006)) or simulation models (Ajose and Mohanty (2003)).
Ide et al. (2007) used simulation model to investigate the impacts of gravity and viscous forces on capillary trapping of CO_2. Results showed that effects of capillary pressure and aquifer inclination increased the amount of CO2 trapped. Hognesen et al. (2006) conducted a series of experiments to identify capillary and gravity dominated flow regimes and concluded that the impact of gravity decreased as the height of the core decreased.

The simultaneous action between capillarity, gravity and viscous forces becomes more complex in fractured geological formation (Berkowitz (2002)).When a wetting fluid

flows through a fracture, capillarity may drives the wetting fluid from the fracture into the matrix, while viscous force propels the fluid to flow through the fracture with less resistance. Rangel-German et al. (2006) stacked Boise sandstone blocks to study multi-phase flow in a fractured system. They concluded that both capillary and viscous force control the flow in the fracture and that capillary continuity can occur in any direction, depending on the relative strengths of the capillary and Darcy (viscous) terms in the flow equations. Tang and Firoozabadi (2000) conducted a series of experiments and found the oil displacement efficiency can be significantly influenced by viscous force and gravity in a fractured porous media. Rangel-German and Kovscek (2002) indicated the effect of gravity on the orientation of fracture-matrix is evident through oil-water experiments. Firoozabadi and Markeset (1992) studied gravity and capillary cross-flow in fractured porous media, and showed that the contribution of capillary cross-flow from the side faces of the matrix rock increased with the tilt angle. Gu and Yang (2003) used numerical modeling to study the interfacial profile between two immiscible fluids in a reservoir with a fracture with random orientation, and found that the equilibrium shape of the interfacial profile depends on the ratio of gravity and capillarity.

Fracture orientation had great influence on fluid displacement under the interplay of capillary, gravity and viscous forces. Crawford and Collins (1954) found the sweep efficiency depends on the length and orientation of the fracture and direction of the flood. Carnes (1966) indicated that it is essential to determine presence and orientation of a fracture system in a reservoir since it has a significant effect on the success or failure of water flooding. Shedid (2006) and Shedid and Zekri (2006) investigated the effect of fracture orientation on water flooding processes. The results indicated fracture orientation had greater influence on oil displacement, and the increase of fracture inclination angle decreases oil displacement by water flooding. Similar experimental work were reported by Farzaneh et al. (2010) recently with different results between the oil displacement and the orientation angle. They conducted experimental studies and observed that the oil displacement decreased when the fractures' aperture, discontinuity, over-lap, and

distribution increased. In contrast, the oil displacement increased when the orientation angle, discontinuity- distribution and the number of fractures increased. However, experimental works addressing the simultaneous action of capillarity, gravity and viscous force under the effect of different fracture orientation (where injection direction is parallel to fracture) is limited. Understanding how these forces affects fracture-matrix transfer mechanisms and how these mechanisms are altered by fracture orientation are of crucial importance and are the main goals of this section.

3.2   Experimental Design

An experimental apparatus including sample holder, fluid supply system and X-Ray CT scanner designed and constructed in the Chapter 2 was used in this study. The rock sample used in this study was Berea Sandstone with average porosity about 22%. A single tensile fracture was created artificially on each disk. Fractures are aligned with the centre of the each sample and are placed perpendicular to the bedding layers. Average fracture apertures are around 0.5mm. Pore volume of the matrix and fracture are 18.51mL and 0.51mL respectively. Five different fracture configurations including (1) horizontal, (2) vertical flowing up,(3) vertical flowing down,(4) diagonal flowing up, and (5) diagonal flowing down were investigated to address the influence of fracture orientation on the capillary imbibition in fractured permeable rock. A detailed matrix of fracture configurations is displayed in Figure 3-1.

Horizontal fracture	Vertical fracture flowing up	Vertical fracture flowing down	Diagonal fracture flowing up	Diagonal fracture flowing down
0°	+90°	+90°	-45°	+45°
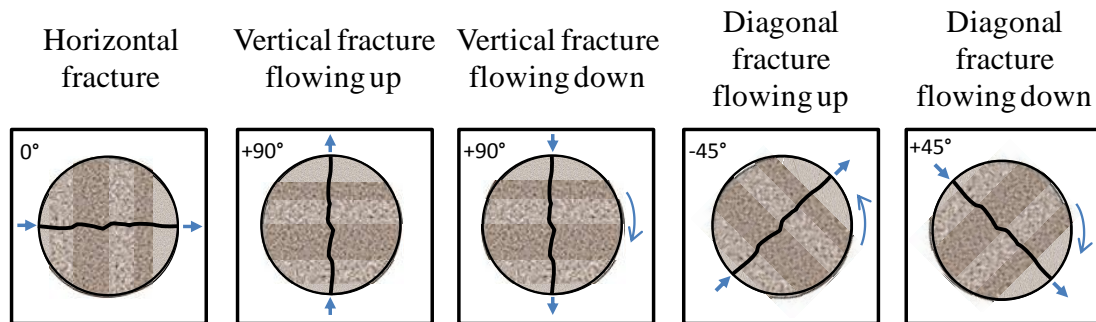
Figure 3-1: Five different fracture configurations.

Air-brine, kerosene-brine and viscous oil-brine represent three different fluid pairs considered in this experimental work. The viscous oil was formed by mixing 50% by weight of n-decane and Silicone oil. Kerosene and viscous oil represent two types of oil phase to pre-saturate the sample. Water was tagged with 15% by weight of sodium iodide (NaI) to increase its CT registration and provide a high contrast between the two phases. The viscosity of tagged water is approximately 1.0 cP and that for kerosene and mixture oil are 2.9 cP and 36.32 cP, respectively. The physical properties of these fluids are shown in Table 3-1.

Before commencing the experiment, wetting and non-wetting liquid phases, were thoroughly mixed with each other and allowed to separate under gravity action. This procedure minimizes in situ changes in saturation due to mutual solubility during the displacement experiment. To guarantee a predominantly capillary-driven displacement, injection flow rates are low, in the order of 4mL/hr, which correspond to capillary numbers (Nca) on the order of 10^{-4} to 10^{-8}. This capillary number represents the relative control of viscous over capillary forces. For capillary numbers below 10^{-5}, flow in porous media is considered to be dominated by capillary forces (Ding and Kantzas (2007)). Bond number (Bo) express the relative importance of gravitational to capillary forces. Table 3-2 summarizes capillary numbers and Bond numbers correspond to three different fluid pairs.

Table 3-1: Physical properties of fluids.

Exp.	Phases	Fluid composition	Viscosity at 25.7^{o}C (cP)	Specific gravity at 25.7^{o}C
Set 1	water	Tagged water(15% NaI by weight)	1.0	1.0
	oil	Kerosene	2.9	0.79
Set 2	water	Tagged water(15% NaI by weight)	1.0	1.0
	Air	Air	0.018	0.001
Set 3	water	Tagged water(15% NaI by weight)	1.0	1.0
	oil	Silicone oil & Decane 50% by weight	36.32	0.83

Table 3-2: Capillary numbers and Bond numbers correspond to three fluid pairs.

	Fluid type	Nca	Bo
Set 1	Kerosene	4.8×10^{-5}	0.038
Set 2	Air	5.5×10^{-8}	0.033
Set 3	viscous oil	2.7×10^{-4}	0.014

3.3   Experiment Procedure and Determination of Porosity and Fluid Saturation

Kerosene-brine and viscous oil-brine follow the same experimental procedure presented in Figure 2-7. Air-brine system shows similar experimental procedure as presented in Figure 3-2. The only difference between these two procedures is, in air-brine system, since distilled water was used to saturate sample for porosity calculations in the stage 2, additional 72 hours vacuuming and air injection was required to drain off water and saturated with air, before starting injection as shown in stage 3.

1. Vacuum sample and scan	2. Saturate sample and scan	3. Drain off distilled water	4. Begin water injection	5. End of water injection
Scan dry slice for fracture identification and rock heterogeneities	Scan slice filled with distilled water. This will be a reference state	Scan slice. This will be an initial condition	Start continuous scanning of slice during water injection	Continue Scanning during water injection

Figure 3-2: Experimental procedure and CT scanning sequence for air-water system.

The average sample porosity (ϕ_{avg}) is about 22% obtained from the volume of fluid used in saturating the sample and the bulk volume of the sample. Pixel porosities (ϕ_{pixel}) were obtained from Equation [2-2] as shown in Chapter 2.4. In situ saturations were also determined using data from the CT scanner. Pixel water saturations ($S_{w,pixel}$) were

obtained from Equation [2-3], $S_{w,avg}$ is the average saturation of water in the sample

obtained from Equation [2-4]. Since initial water saturation exist in all air-brine

experiments, in situ saturations and average saturations need to be modified as presented

in Appendix A.2 Equation [22] and Equation [33].

3.4   Results and Discussions

3.4.1   Impact of Viscosity Ratio

In this section, we compare three different immiscible fluid pairs with different viscosity

ratios using the same injection flow rate of q=4ml/hr in horizontal fractured rock samples.

In experiment set 1, the sample was pre-saturated with kerosene; in experiment set 2, the

sample was pre-saturated with air; and in experiment set 3, the sample was pre-saturated

with viscous oil before starting brine injection. Figure 3-3 presents average saturation

changes as a function of time for all case. These saturations were averaged over the entire

sample, including fracture and rock matrix. In Figure 3-3, we can see the difference in

water saturation as a function of time and pore volume injected (PVI) for the three fluid

pairs under consideration. Since the existence of initial water saturation (Swi=0.1225) in

set 2, air-brine, initial saturations for set 2 is higher than set 1 and set 3 as shown in blue

diamond of Figure 3-3-top. In order to compare these saturation curves under the same

start point, pore volume injected (PVI) for set 2 was extrapolated to zero, as shown in

Figure 3-3-bottom. The results show that early time behavior is nearly identical for set1

and set 2, because this is controlled by the injection rate that has been specified as 4

mL/hr. After around 0.4 PVI, set 2 begins to separate from set 1 and reaches maximum

water saturation at an earlier time. In addition, set 2 increases as a straight and overlaps

the line of constant imbibion rate implying water saturation increases as a constant rate.

While for set 3, water saturation is negligible during the first 700 minutes of injection,

and increases up to 0.1 after 4000 minutes of continuous injection. The increment in

water saturation from set 1 and set 2 is much faster, displaying the influence of viscous

forces.
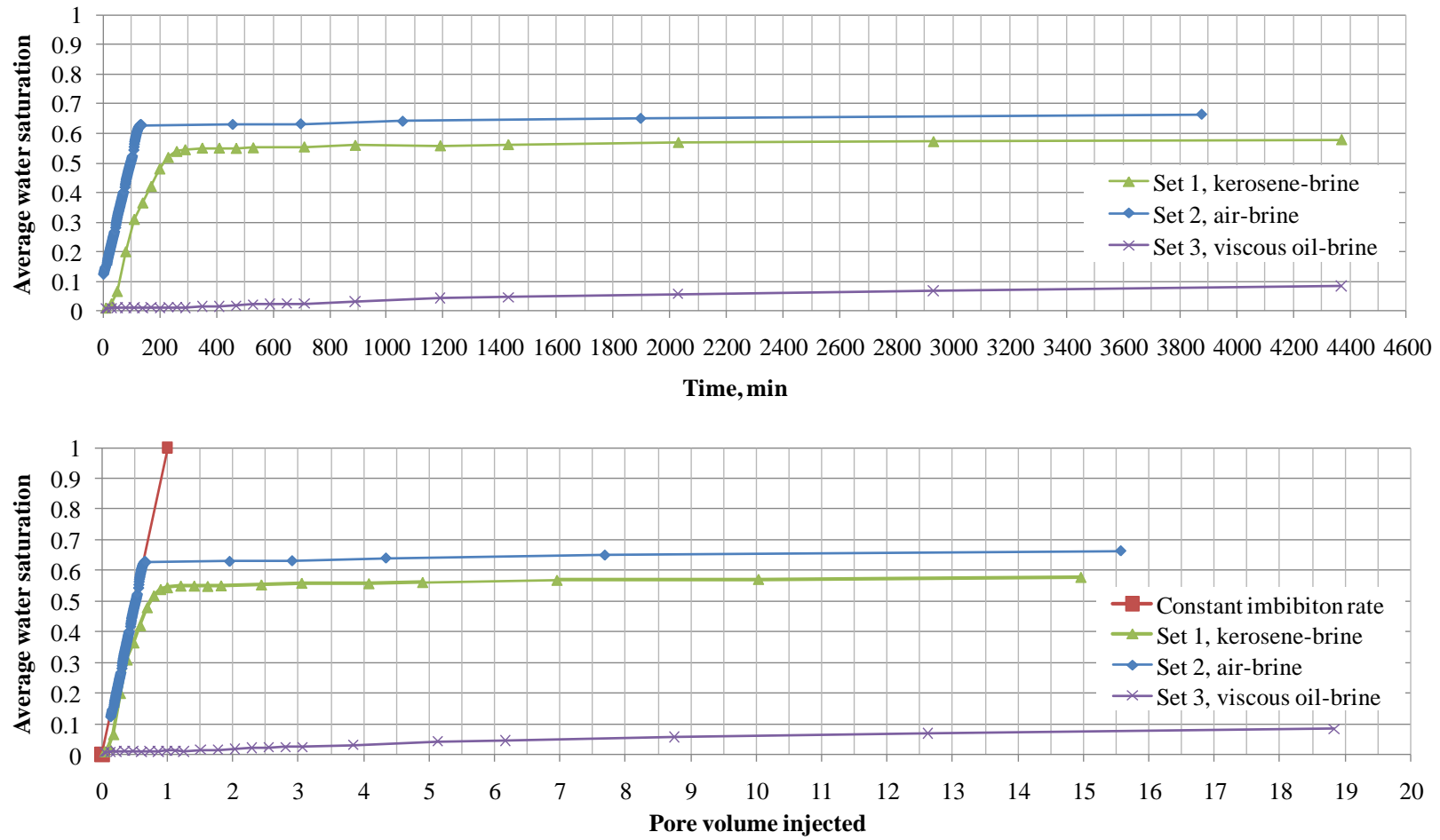
Figure 3-3: Average water saturation as a function of time and PVI for different fluid pairs.

The time progression of water saturation maps corresponding to three fluid pairs are presented in Figure 3-4. Dark blue represents regions saturated with kerosene (Sw=0.0), red represents regions saturated with water (Sw=1.0), and intermediate colors represent the co-existence of kerosene and water. A late water breakthrough time, 0.54 PVI (135 minutes), is observed in set 2 (the case of water displacing air), while an early breakthrough time, 0.03PVI (10 minutes), is observed in set 1 (the case of water displacing kerosene). In addition, a co-current flow mechanism can be observed in set 2 where water and air toward a same direction, while a counter-current flow mechanism where water and kerosene moving in an opposite direction was observed in set 1. This is because a relative smaller viscosity ratio and higher interfacial tension in set 2 (the case of water displacing air) than that in set 1 (the case of water displacing kerosene) that makes injected water more easily flow from the fracture into the matrix; thus delaying water breakthrough time and displaying as co-current flow mechanism. In addition, in set 2, fracture-matrix transfer mechanism switches from co-current to counter-current imbibition after water breakthrough, thus limiting additional recovery of the resident fluid phase as shows in Figure 3-3 (after 135 minutes) and Figure 3-3 (after 0.54 PVI). That is consistent with our knowledge that co-current imbibition can be a more efficient displacement than counter-current flow (Pooladi-Darvish and Firoozabadi (2000)). In set 3, there is only a little increase in water saturation in the neighborhood of the fracture for the first 300 minutes; however, none in the matrix. After 1440 minutes, the brine starts to accumulate in the fracture, represented by the red shades. Under this flowing condition, there is no evident matrix-fracture transfer or imbibitions into the rock matrix. The oil in the fracture is displaced by brine due to forced injection.

Close examination of Figure 3-5 reveals similar observation through vertical saturation profiles. These vertical saturation profiles averaged over the central 6 mm of each CT slice for three different fluid pairs. These profiles capture saturation changes with time in the direction perpendicular to the fracture. For all experiments, continuous high water saturation is observed at the center of the sample (0mm, or fracture location). In

experiment set 2, the saturations appear after 60 minutes of water injection, while a sharp water saturation peak along the fracture is observed in the early time of set 1(t=20 minutes). That is consistent with a late water breakthrough time in experiment set 2 and an early water breakthrough time in experiment set 1 observed in Figure 3-4. In set 3, there is only a saturation peak in the fracture, and no water in the matrix implying that capillary forces are not strong enough to drive brine into the matrix and displace the resident viscous oil, thus making the overall process viscous dominated.
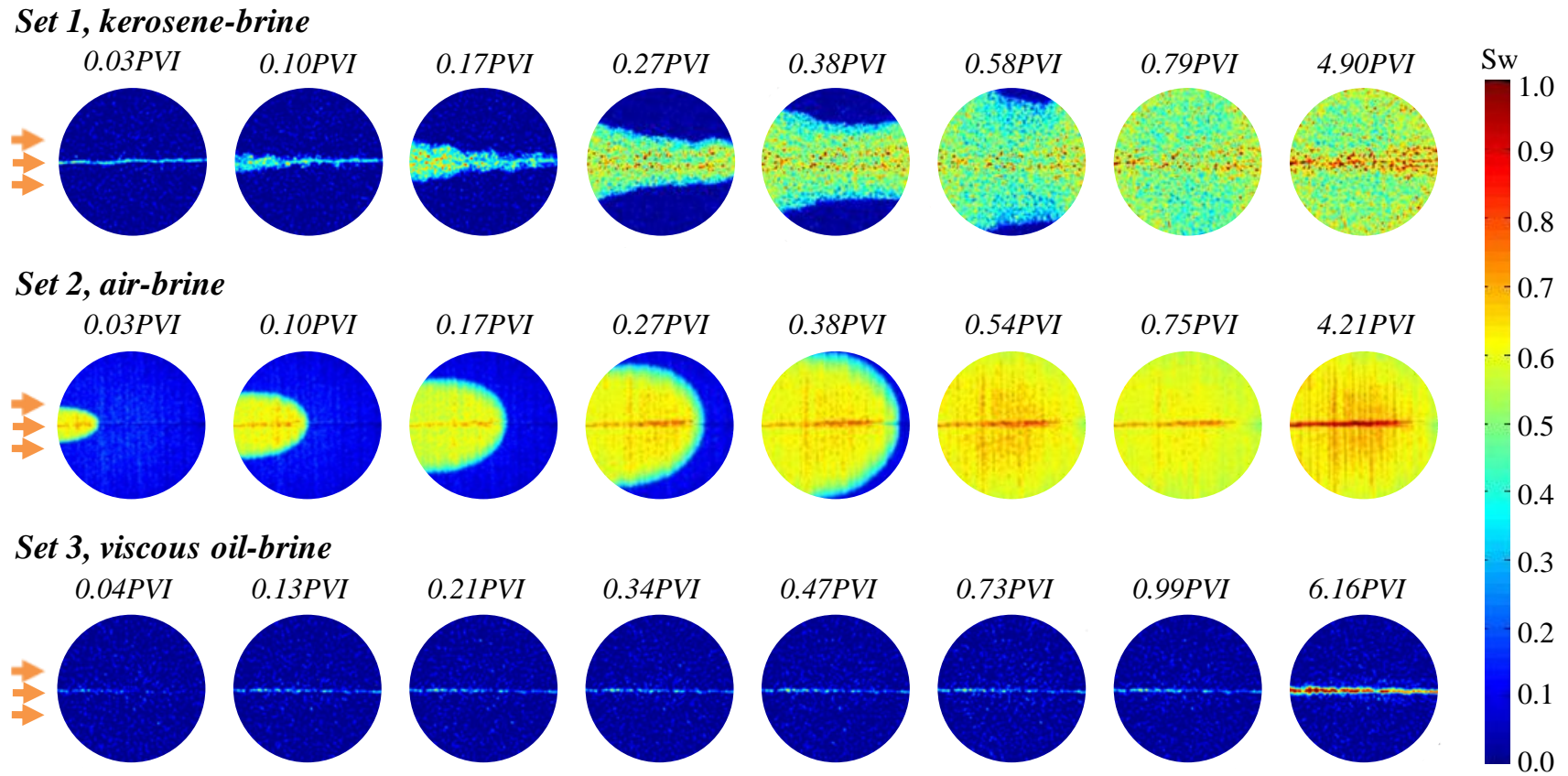
Figure 3-4: Sequence of water saturation maps obtained from CT scanning at 4mL/hr water injection rate for different fluid pairs.

Figure 3-5: Vertical Saturation profiles perpendicular to the fracture and averaged over the central 6 mm of the sample, for different fluid pairs.

3.4.2   Impact of Fracture Orientation

In this section, we compare five different fracture orientations in the case of water displacing air using same injection flow rate q=4ml/hr as displayed in Figure 3-1, including:

(1) horizontal fracture.

(2) vertical fracture flowing up.

(3) vertical fracture flowing down.

(4) diagonal fracture flowing up.

(5) diagonal fracture flowing down.

Figure 3-6 shows average water saturation as a function of pore volume injected (PVI) for these five different fracture orientations. Once again, early time behavior is nearly identical for all cases, because this is controlled by the injection rate that has been specified as 4 mL/hr. After around 0.62 PVI, different cases start to separate from each other. The cases of horizontal fracture and vertical fracture flowing down begin to separate first and reach the lowest final saturation value at about 0.6-to-0.7 after 15 PVI. On the contrary, diagonal fracture flowing up and vertical flowing up show later breakthrough and higher ultimate saturation value after 15 PVI. The ultimate recovery from these imbibition scenarios is primarily controlled by breakthrough time, when the flow mechanism switches from co-current to counter-current, thus limiting extended recovery of the resident fluid phase.

 The time progression of water saturation maps corresponding to these five fracture configurations are presented in Figure 3-7. A co-current flow mechanism prevailed in all cases when displacing a non-wetting gas phase confirming previous observation in Chapter 3.3.1 (impact of viscosity ratio) that co-current flow dominates in the case of water displacing air due to a relative smaller viscosity ratio and higher interfacial tension. In addition, the water front in the matrix is moving faster than that in the fracture, which
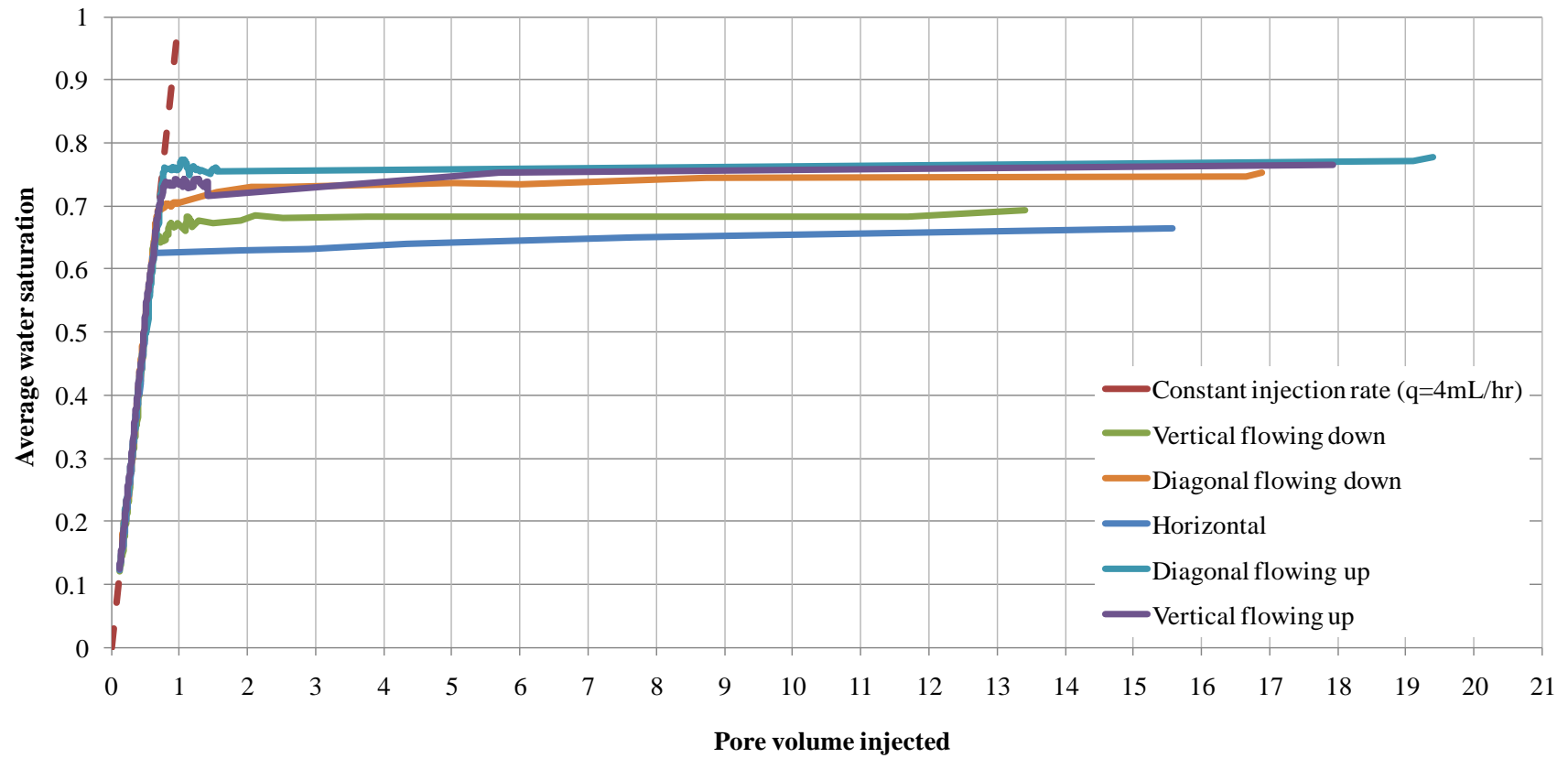
Figure 3-6: Average water saturation as a function of pore volume injected (PVI) for different fracture orientations.
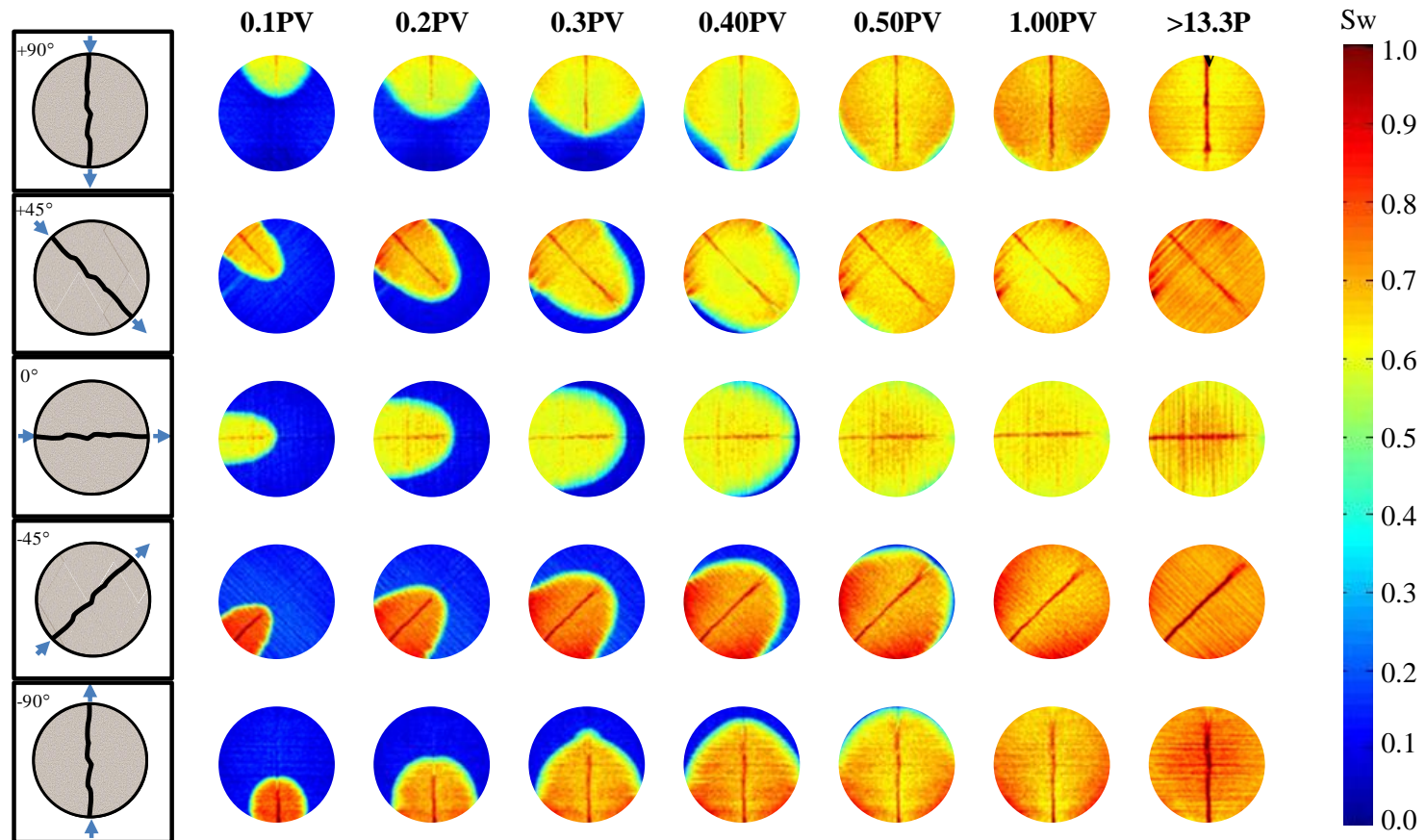
Figure 3-7: Sequence of water saturation maps obtained from CT scanning at 4mL/hr water injection rate for different fracture orientations.

indicates that capillary force in the matrix is larger than that in the fracture. This observation is evident as a shorter red line in the fracture zone within the imbibing front in Figure 3-7.

The existence of rough-walled fractures and a relative faster moving rate of the water front in the matrix than fracture also contribute to snap-off effects. There is direct evidence of snap-off inside the fracture when the invading front in the matrix moves ahead of the invading front in the fracture which leads to an air bubble was trapped behind the water front in fracture zone as shown in Figure 3-8. This phenomena occurs when the capillary pressure decreases or the radius of the curvature of the water (wetting-phase fluid) increases and the water layers in the aperture start to swell and temporary cut off the connection of air phase.
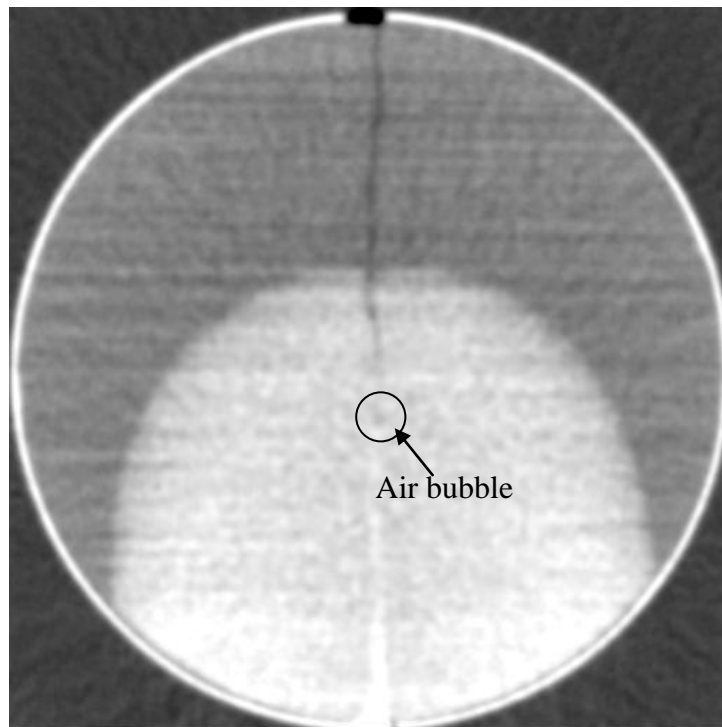
Figure 3-8: Saturation maps showing air (circular shadow) trapped in the fracture zone as water injected time equals to 61 minutes.

Figure 3-9 shows snapshots of a generation of snap-off. An air bubble was trapped in the fracture zone when water injected time equals to 61 minutes. However, this balance did not hold for a long time. After one minute of continuous injection, this air bubble erupted, and at the same time, it changed the shape of water front as water injected time equals to 62 minutes and the water front extended following this flow intermittency

| (60min) | (61min) | (62min) | (63min) | (64min) | (65min) | (66min) |
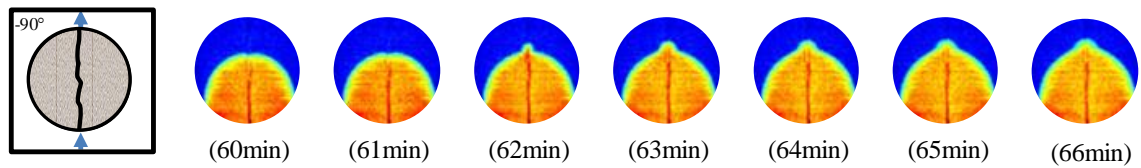
Figure 3-9: Saturation maps showing air snap-off in the fracture.

The influence of fracture orientation resulting in different water breakthrough time can be observed at PVI=0.4 (time=135minutes) where late water breakthrough can be discovered in the case of diagonal fracture flowing up and vertical fracture flowing up. In addition, higher water saturations represents in darker red can be observed behind imbibing front in the case of diagonal fracture flowing up and vertical flowing up as shown in Figure 3-7. This is because gravity slightly delays the progression of water imbibing front and water breakthrough time, thus more water was accumulated behind water front.

Similar observations are made from the vertical saturation profiles in Figure 3-10. A higher water saturation value at the same PVI and slower water front evolving can be observed in the Figure 3-10-right when PVI=0.2. In addition, a higher final water saturation value can be observed in the fracture zone of Figure 3-10 right when PVI=17.8.
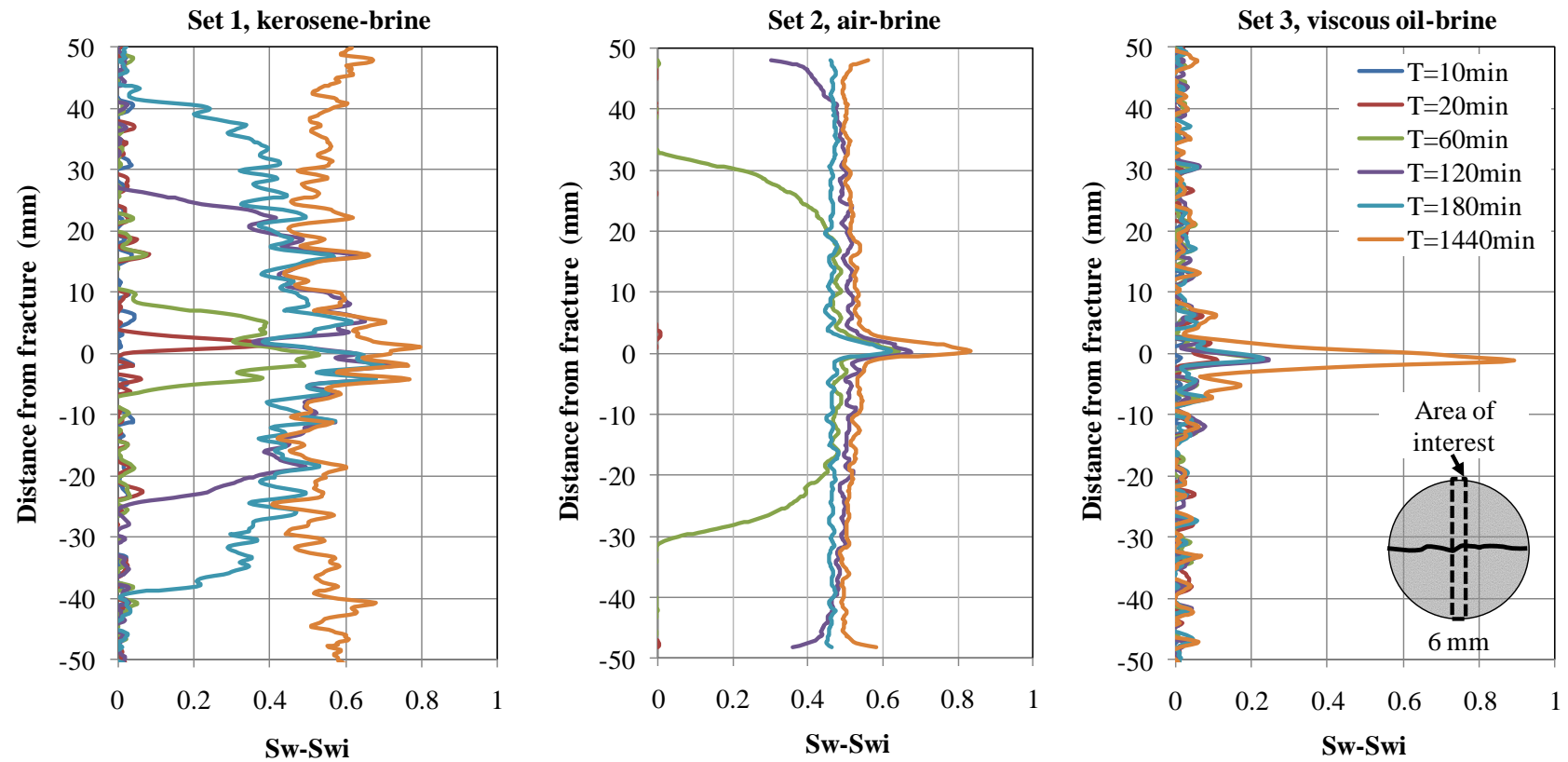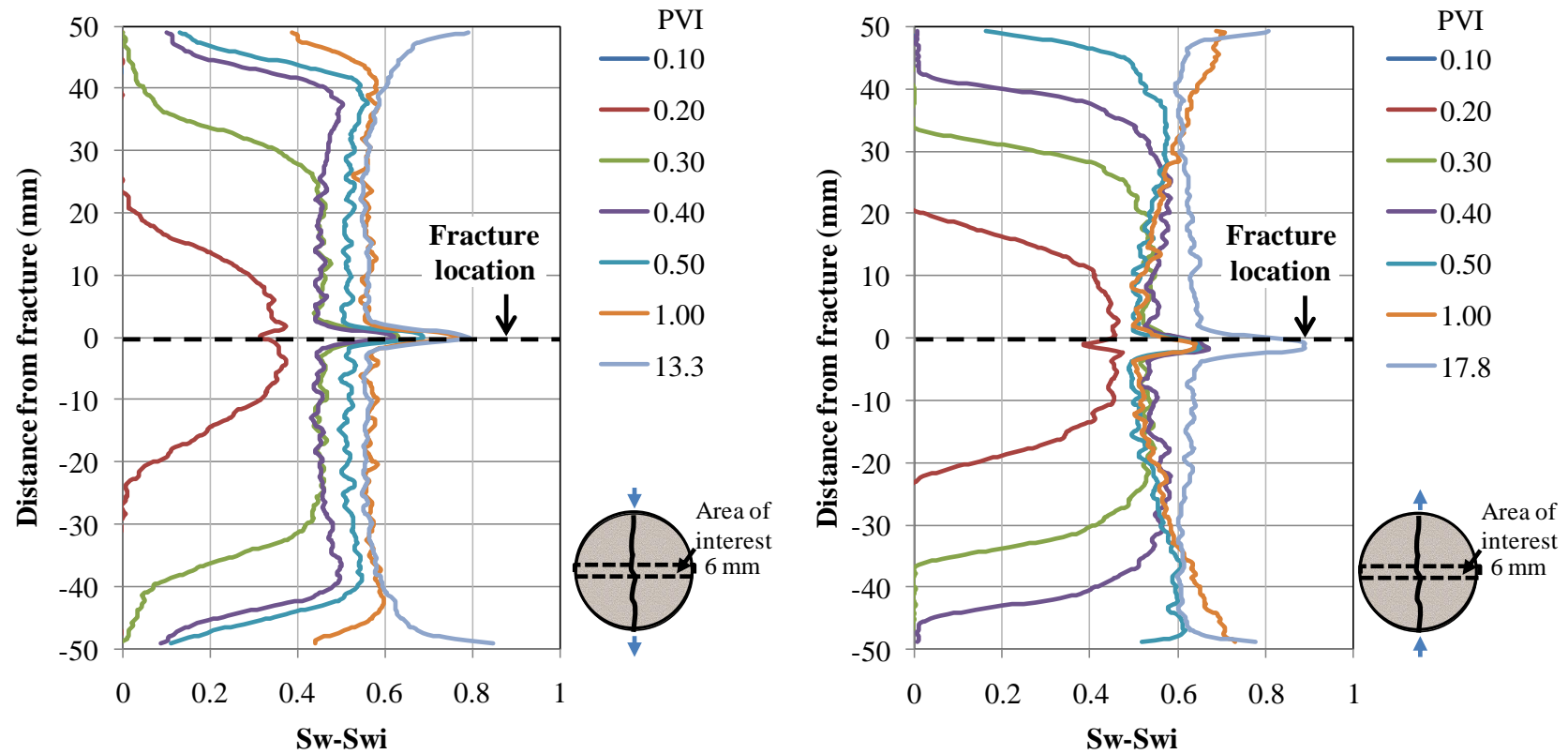
Figure 3-10: Vertical Saturation profiles perpendicular to the fracture and averaged over the central 6 mm of the sample, in the case of vertical fracture flowing down and vertical fracture flowing up.

Chapter 4

Numerical Analysis of Imbibition Front Evolution and History Matching

Appropriate transport properties such as relative permeability and capillary pressures are essential for successful simulation and prediction of multi-phase flow in such systems. However, the lack of thorough understanding of the dynamics governing immiscible displacement in fractured media limits our ability to properly represent their macroscopic transport properties. In this study, an automated history matching approach proposed by Basbug and Karpyn (2008) was implemented to generate representative matrix and fracture relative permeability and capillary pressure curves Sequential saturation distribution maps of brine displacing kerosene at low injection rate (4mL/hr) presented in Chapter 2 were used as matched data. These optimized curves were then validated with previous experimental data at higher water injection rate (40mL/hr) condition. Sensitivity analyses were performed in order to study the effects of transport properties and boundary effects on oil displacement and water front evolution. Through this study, significant insight is provided for transport properties on the water front progression in fractured permeable systems under capillary dominated conditions.

4.1   Literature Review

Transport properties such as permeability and capillary pressure are important for successful description of fluid displacement processes (De la Porte et al. (2005)). Numerous papers had proposed techniques for estimation of relative permeability and capillary pressure curves for both matrix and fracture by using experiments or simulation models. Heaviside et al. (1983) determined representative relative permeability and capillary pressure curves using both steady-state and unsteady-state experiments as well as numerical modeling. Firoozabadi and Hauge (1990) proposed a phenomenological

model to relate the fracture capillary pressure to saturation. El-Khatib (1995) developed a modified J-function for calculating capillary pressure. Mohamad Ibrahim and L.F. Koederitz (2001) presented a relative permeabilty prediction model from two phase steady-state and unsteady-state experiment data. Bertels et al. (2001) developed an experimental technique to measure and compute fracture aperture distribution, capillary pressure, and relative permeability in fractured rocks using X-Ray CT scanning. Li (2008) and Li and Horne (2010) generated a correlation between resistivity index with relative permeability and capillary pressure data.

Kruger (1961) first applied history matching technique to calculated the areal permeability distribution of the reservoir. Archer and Wong (1973) and Chavent et al. (1980) applied similar approach to obtain relative permeability as well as capillary pressure curves curves from experimental data. With the improvement of technology, this technique becomes feasible to obtain permeability and capillary pressures curves. Chen et al. (2005) developed optimization code based on Levenberg-Marquardt algorithm and coupled it with a commercial reservoir simulator to match well test data and obtain relative permeability curves. Basbug and Karpyn (2008) proposed a history matching approach can automated determine both matrix and fracture relative permeability and capillary pressure curves using B-spine equations. Angeles et al. (2010) developed history matching model for relative permeability curves and capillary pressure curves using field test data including resistivity, pressure and flow rates.

In order to accurately simulate and predict fluid transport behavior through fractured systems, a thorough understanding of the variables that affect fluids transport through fractures is necessary. Al-Wadahi et al. (2000) and Li (2003) applied of history matching technique to investigate three phase counter-current flow mechanism. Similar study was done by Alajmi (2003) to investigate the influence of a fracture tip on two-phase flow displacement processes. Or (2008) indicated key factors shaping the displacement front morphology, including fluid velocity, density and viscosity ratios, interfacial tensions,

and pore size distribution of the porous medium. Tavassoli et al. (2005a, b) proposed an approximate analytical approach to analyze capillary force counter-current imbibitions in both strongly and weak water-wet systems to assist dual-porosity modeling of flow in fractured reservoirs. Rangel-German and Kovscek (2005) found that relative permeability for fractured rocks with impermeable matrices are different from those for fractured porous rocks. Relative permeability curves for fractures not interacting with granular matrices are represented by X-type functions, while relative permeability for fractures interacting with porous matrices do not necessary exhibit X-type behavior. The shape of this function is controlled by injection flow rate, fracture aperature and the imbibition potential of the rock.

However, analyzing the relationship between transport properties and water font morphology especially under capillary dominated condition within fractured system, remains largely unexplored, and is the main goal of this section. Results from this work help visualize the impact of transport properties on the water front progression and, at the same time, provide detailed quantitative information for the simulation and prediction of multiphase flow in fractured permeable systems.

4.2 Automated History Matching Approach

History matching is a technique that adjusts simulation parameters until they are able to reproduce the "history" of the modeled system. In this study, an automated history matching approach proposed by Basbug and Karpyn (2008) was implemented and to execute this matching approach. This code was developed under MATLAB® 2006b with the optimization algorithm and coupled with the commercial reservoir simulator. The B-spline functions used for determining relative permeability curves and C++ programming code used for extracting saturation data from the simulator output results were replaced by modified Brooks and Corey equations and a MATLAB® subroutine code to simplify and accelerate simulation speed.

A schematic diagram of automated history matching approach is illustrated in Figure 4-1. The process starts with a reasonable initial guess of rock and fluid properties including relative permeability and capillary pressure. The black oil module (IMEX (2009)) of a commercial reservoir simulator (CMG) were use to run the simulation. Saturation distribution were then extracted from the output results and compared with the experimental data. Matrix and fracture relative permeability and capillary pressure curves were then updated with a large-scale optimization algorithm (Trust-Region Method) if the difference between experimental and simulation results did not fall within prescribed error bounds. Large-scale optimization (Trust-Region Method) is an algorithm that minimizes the least-squares objective function, J is implemented for adjusting. The objective function is given by:

$$J = \sum_{\Omega(x,y,z,t)} \left(S^{cal}_{x,y,z,t}(k_r, P_c) - S^{exp}_{x,y,z,t} \right)^2 \quad \text{...[4-1]}$$

where $S^{cal}_{x,y,z,t}$ is the saturation results calculated from simulation, while $S^{exp}_{x,y,z,t}$ is that obtained from previous experiment.

Initialization

| Initialize Control Parameters | → | Define Flow Properties | → | Prepare Input Files |

Simulation

| Run Reservoir Simulator | → | Determine Saturation Distribution (S_{cal}) |

Convergence

| Convergence Check $J=\sum(S_{cal}-S_{exp})^2$ | —Yes→ | Report Reservoir Flow Properties |

↓ No

Large-scale Optimization

| Adjust Control Parameters | → | Re-define Flow Properties | → | Prepare New Input File |

Basbug and Karpyn (2008)

Figure 4-1: Schematic diagram of history matching approach (Basbug and Karpyn (2008)).

The dimension of the experimental work in Chapter 2 was 485×485 pixels with the resolution approximate 0.205mm (105mm/512). An up-scaling scheme was applied to increase speed on both simulation and optimization process. For that purposes, experimental data (saturation images) was up-scaled by a factor of 5 in each direction using the arithmetic average. This factor is based on the fracture aperture resolution suggested by Glass et al. (1998), and correlation length suggested by Keller (1998)). After up-scaling scheme, simulation model dimension became 97×97 pixels with approximate resolution 1.025mm (525 mm/512). This dimension was also applied to following simulations including sensitivity analysis, automatic history matching approach and predicted simulation studies.

The shape of the modeled system is a circular disk with diameter of approximate 99.463mm (50925 mm/512) and thickness of 10 mm. A continuous fracture layer is positioned along in the center of the simulation model. The initial water saturation was zero before starting water injection. We used constant flow rate inlet, 4mL/hr and constant pressure outlet along with no flow boundary condition for the entire model. The inlet and outlet were located at start and end of the fracture layers respectively.

Porosity distributions were extracted from experimental work in Chapter 2 and up-scaled by a factor of 5 in each direction by using the arithmetic average.

Absolute permeability, k in each pixel was obtained from equation Timur's correlation (Timur (1968)), given by:

$$k = 0.136 \cdot \frac{\phi^{4.4}}{S_{wirr}^{2}} \quad \text{..} \quad [4\text{-}2]$$

where ϕ is the pixel porosity of the rock sample (percentage) obtained from experimental work in Chapter 2, and S_{wirr} is the irreducible water saturation (fraction).

Table 4-1 presents a summary of porosity and permeability values used in the present simulation model. Relative permeability and capillary pressure curves are defined with modified Brooks and Corey equation (Lake (1989)), given by

$$k_{rw}(S_w) = k_{rw}^o \cdot (S_{wn})^{Nw} \quad\text{..}\quad [4\text{-}3]$$

$$k_{ro}(S_w) = k_{ro}^o \cdot (1 - S_{wn})^{No} \quad\text{..}\quad [4\text{-}4]$$

$$P_c(S_w) = \frac{P_{ce}}{(S_{wn})^{0.5}} \quad\text{..}\quad [4\text{-}5]$$

$$S_{wn} = \frac{S_w - S_{wirr}}{1 - S_{or} - S_{wirr}} \quad\text{..}\quad [4\text{-}6]$$

where S_w is water saturation, k_r is relative permeability, P_c is capillary pressure, S_{wirr} and S_{or}, were irreducible water saturation and residual oil saturation; end-point relative permeabilities are identified with the superscript symbol "o" obtained from perious steady-state relative permeability experiment. n_o and n_w are Corey exponent to oil and water respectively. P_{ce} is capillary entry pressure.

Table 4-1: Rock properties assigned to fracture and matrix in simulation model.

Property	Value
Fracture permeability [md]	5000
Average matrix permeability [md]	76.5
Fracture porosity [fraction]	0.3262
Matrix porosity [fraction]	0.2273

4.3 Sensitivity Analysis

To explore the sensitivity of imbibition front development to fracture/matrix transport properties, we have constructed a series of test cases including sensitivity to matrix relative permeability as well as matrix and fracture capillary pressure curves according to the following case studies. All modified transport properties are listed in Table 4-2.

Case A: reference case.

We used base-case transport properties provided in Figure 4-2. Model dimensions, porosity and absolute permeability distributions, flowing conditions and fluid properties were as presented in Chapter 4.2 (page 41 through 43).
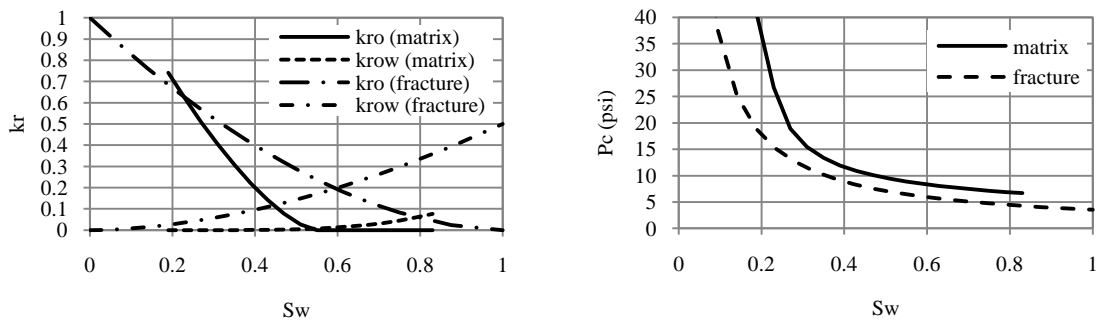
Figure 4-2: Matrix and fracture relative permeability curves (left) and capillary pressure curves (right) used in sensitivity analysis case A.

Table 4-2: Lists of investigated parameters in sensitivity analysis cases.

Case	Corey exponent oil (n_o)	Corey exponent water (n_w)	End-point relative permeability (k^o_{rw})	Matrix capillary entry pressure (P_{ce})
A	8	2.5	0.077	24.5
B	2	2.5	0.077	24.5
C	8	4	0.5	24.5
D	8	2.5	0.077	3.8

Case B: sensitivity to relative permeability to oil in the rock matrix.

To investigate the sensitivity of front evolution to matrix oil relative permeability (k_{ro}), we increased relative permeability to oil by decreasing Corey exponent oil (n_o), to compare cases A ($n_o = 8$) and B ($n_o = 2$), see Figure 4-3.
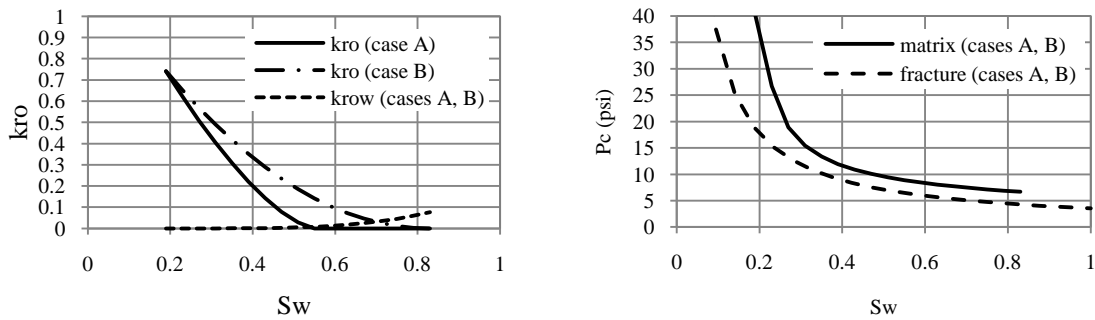
Figure 4-3: Matrix relative permeability curves (left) and capillary pressure curves (right) for sensitivity analysis cases A, B.

Case C: sensitivity to relative permeability to water in the rock matrix.

To investigate the sensitivity to matrix relative permeability to water (k_{rw}), we increased water relative permeability by Corey exponent water (n_w) and increasing end-point relative permeability (k_{rw}^o), to compare cases A ($n_w = 2.5$, $k_{rw}^o = 0.077$) and C ($n_w = 4$, $k_{rw}^o = 0.5$), see Figure 4-4.
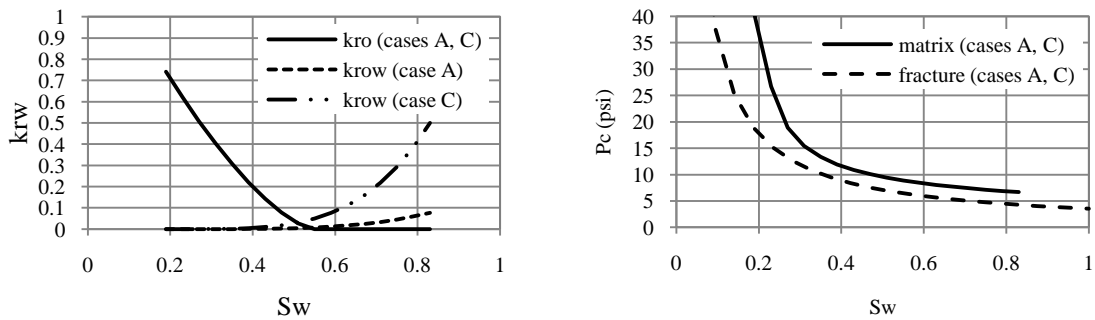
Figure 4-4: Matrix relative permeability curves (left) and capillary pressure curves (right) for sensitivity analysis cases A, C.

Case D: sensitivity to capillary pressure contrast between matrix and fracture.

To investigate the sensitivity to capillary pressure contrast between matrix and fracture, we decrease capillary entry pressure (P_{ce}) in the fracture to compare cases A ($P_{ce} = 24.5$) with D ($P_{ce} = 3.8$), see Figure 4-5.
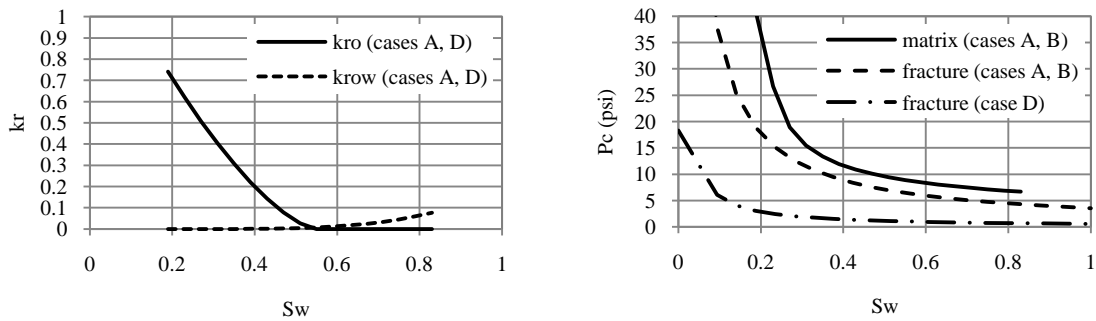
Figure 4-5: Matrix relative permeability curves (left) and capillary pressure curves (right) for sensitivity analysis cases A, D.

Simulation results of imbibition front evolution in fractured sandstone were compared and analyzed based of average water saturation (Figure 4-6), water saturation maps as a function of time (Figure 4-7), and water saturation profiles perpendicular to the fracture (Figure 4-8). Figure 4-6 presents average saturation changes as a function of time for all cases. These saturations were averaged over the entire sample, including fracture and rock matrix. Early time behavior is nearly identical for all cases, because this is controlled by the injection rate that has been specified as 4 mL/hr. After around 80 minutes of injection, each test case begins to separate from the reference case A. Cases B, C and D reach higher water saturation faster, and thus higher oil displacement, than case A, implying more mobile oil and water phases inside the modeled system. Notice that an increase in matrix relative permeability (cases B and C) or capillary pressure contrast between matrix and fracture (case D), can lead a faster oil displacement rate. At a water saturation of about 0.56, oil displacement becomes negligible in cases A, C and D;

however, in case B, saturation keeps increasing until 0.8, which is consistent with a larger mobile region in the transport properties specified for case B.
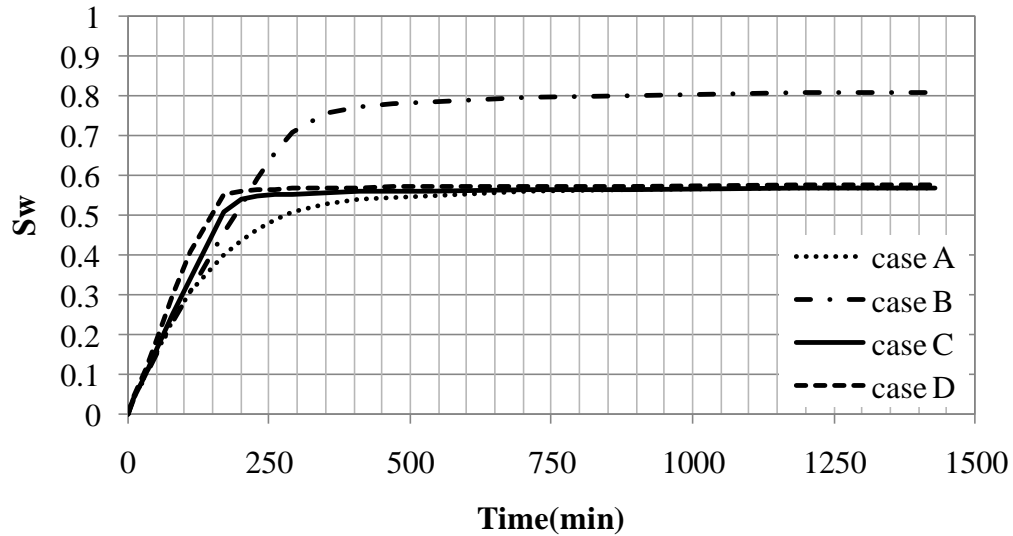
Figure 4-6: Average water saturation as a function of time for sensitivity cases A, B, C and D.

Figure 4-7 shows time progressions of water saturation (Sw) maps for cases A through D. Red represents regions saturated with water (Sw=1.0), dark blue represents regions saturated with kerosene (Sw=0.0), and intermediate represent the co-existence of kerosene and water. In Figure 4-7, case A, base case, an early water breakthrough was observed. Under this flowing condition, the fractures refills with water at a faster rate than it can be transferred through the fracture-matrix interface, confirming similar experimental observations found in the literature (Rangel-German and Kovscek (2002)). Simultaneously, counter-current imbibition is occurring in the water invaded zone as oil is expelled from the matrix into the fracture. As time progresses, the imbibition front moves away from the fracture, and water accumulation becomes evident in the fracture zone in red, supporting the fact that the rate of capillary dispersion through the matrix is low compared to the rate of injection.
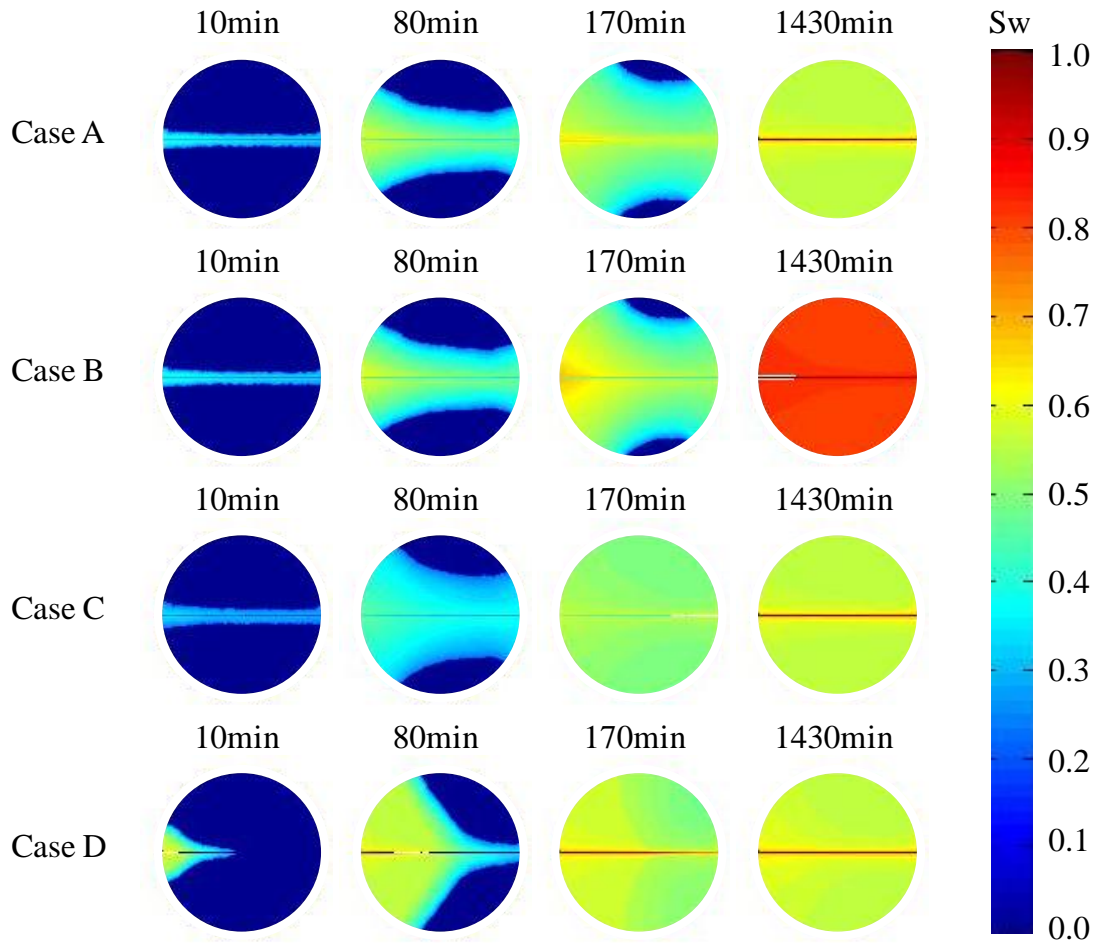
Figure 4-7: Sequence of water saturation maps at 4mL/hr water injection rate for sensitivity cases A, B, C and D.

In cases B and C, where oil and water matrix relative permeability curves were increased relative to the reference case A, early water breakthrough and counter-current flow mechanism were also observed. However, a higher final water saturation can be observed in case B, as time equals to 1430 minutes. This observation confirm a previous finding in Figure 4-6, due to a larger mobile region for oil phase in the transport properties specified for case B, final water saturation can keep increasing until 0.8.

In case C, where matrix relative permeability to water has been increased, we observe a faster water front extension as it spreads away from the fracture when time equals both 80 and 170 minutes. This is because of the wider mobile range for the water phase in the transport properties specified for case C, which make the injected water more mobile at low saturation. However, because matrix relative permeability to oil in cases A and C, the increased matrix relative permeability to water can only enable the water front to extend farther into the matrix instead of increasing the average water saturation in the sample.

In case D, there is a significant difference in the shape of the imbibition front due to increased capillary pressure contrast between matrix and fracture. We also observe a delayed water breakthrough in case D. This form of imbibition front evolution is characterized by an early period of co-current displacement until water breakthrough, followed by counter-current imbibition. In this case, due to higher capillary pressure contrast between fracture and matrix, injected water is more easily derived from the fracture, and thus delaying its breakthrough time, presenting an inclined shape of water fronts, and a higher water saturation value behind water front as shown in yellow as 80 minutes of Figure 4-7 case D.

Further quantitative examination of saturation changes for cases A through D is presented in Figure 4-8. These are vertical saturation profiles average over the central 6 mm of the simulation model, which capture saturation distribution at 80 minutes of injection, in the direction perpendicular to the fracture. As shown in Figure 4-6, all cases reach almost the same average saturation value after 80 minutes of injection. Under this time frame, an increased oil relative permeability in the matrix (case B) shares a similar vertical saturation profile with the reference case A, as shown in Figure 4-8, representing a similar imbibition rate from the fracture into matrix.
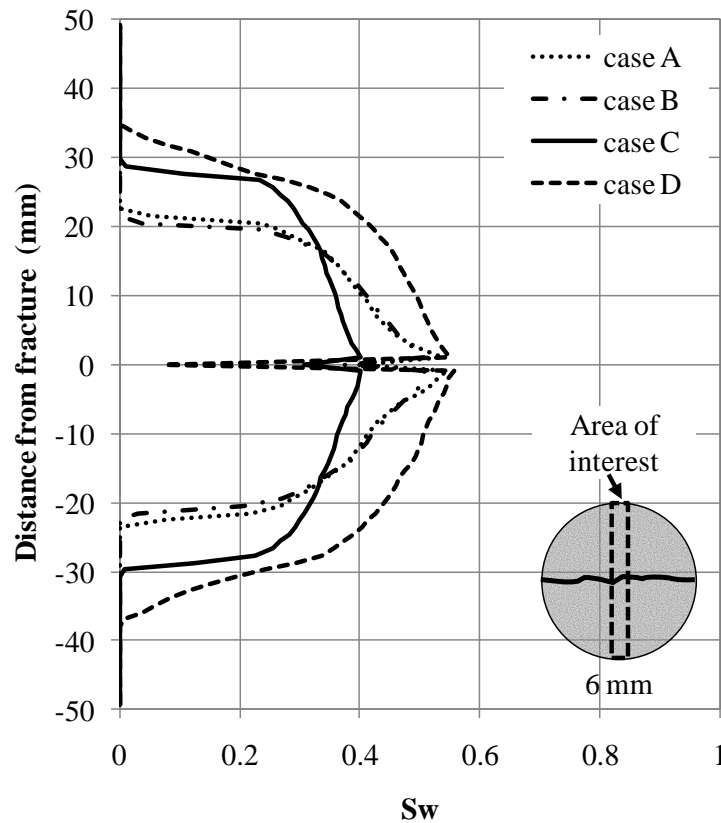
Figure 4-8: Vertical saturation profiles perpendicular to the fracture and averaged over the central 6 mm of the simulation model, q=4mL/hr at time=80 minutes for sensitivity analysis cases A, B, C and D.

However, an increase in water relative permeability (case C) tends to lead a much broader water front progression, and consequently decreases the amount of water saturation in the fracture zone. In addition, this extension changes saturation gradient, causing a drastic drop in saturation across the water front. The same phenomenon is demonstrated in the plot presented in Figure 4-9, where the loss of color contrast behind the water front was observed with increasing the water front progression to matrix system in case C. In case D, the increased capillary pressure contrast between matrix and fracture creates an even broader water front, which is consistent with early observations of higher oil displacement rate and inclined shape of water fronts in Figure 4-7. It is therefore

proved that either water relative permeability or capillary pressure contrast can increase mobility of water phase, and thus influence the speed of water front extension, while the relative permeability to oil primarily controls residual saturations at the end of the displacement process. The balance of capillarity and relative permeabilities also has a significant impact of the shape of the invasion front, resulting in periods of co-current and counter-current imbibition.

4.4 History Matching Results and Validation

The purpose of this section is to determine the representative transport properties using the proposed automated history matching method, and hence could be readily adapted for its application to the analysis of additional predictive scenarios. A sequential saturation distribution maps at low water injection rate (4mL/hr) was used as matched data to generate representative relative permeability and capillary pressure curves. Based on the observations from the experiments and sensitivity analysis, an appearance of early water breakthrough and counter-current imbibition should be observed throughout the simulation. Average saturation as a function of time, spatial saturation profiles, and visual inspection of imbibition front are used as additional agreement criteria to generate a robust history matching result. These optimized curves were then validated with previous experimental data at higher water injection rate (40mL/hr) condition. Three further simulations were used to investigate the effect of homogeneity, heterogeneity and shape of boundary condition on the imbibition front evolution.

Relative permeability and capillary pressure curves after history matching approach are shown in Figure 4-9 and Figure 4-10. Figure 4-9 indicates that relative permeability curve in fracture is larger than that in matrix, while capillary pressure in matrix is higher as shown in Figure 4-10. The relative permeability ratio between oil and water phase (kro/krw) is close to 0 as water saturation equals to 0.55 implying oil displacement rate starts to slow down after that point. In addition, matrix relative permeability curves

intersect at a water saturation of 0.53, which is consistent with experimental observation of a dynamic equilibrium between oil and water phases within the imbibed zone at Sw=0.50-to-0.55. (Lee and Karpyn (2010)).
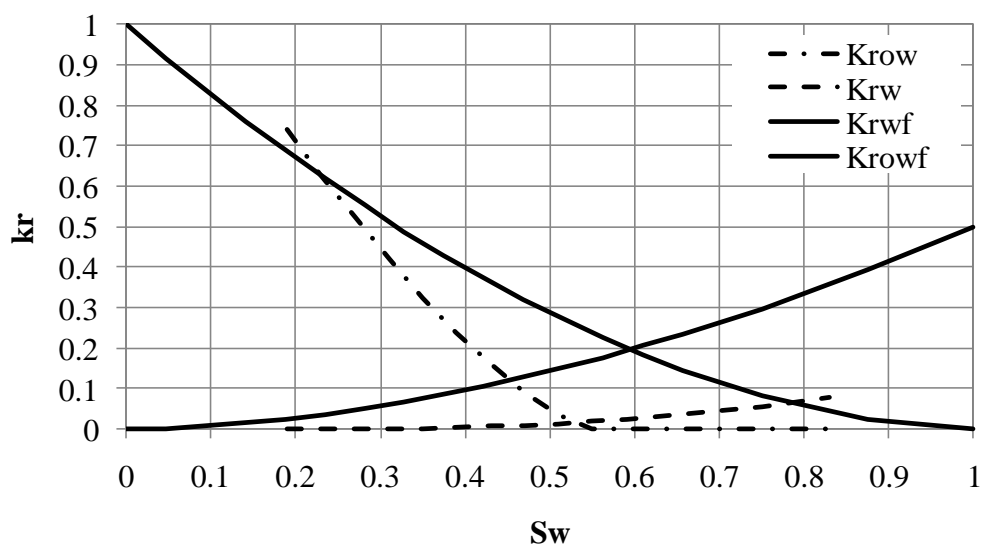
Figure 4-9: Matrix and fracture relative permeability curves obtained from history matching method.
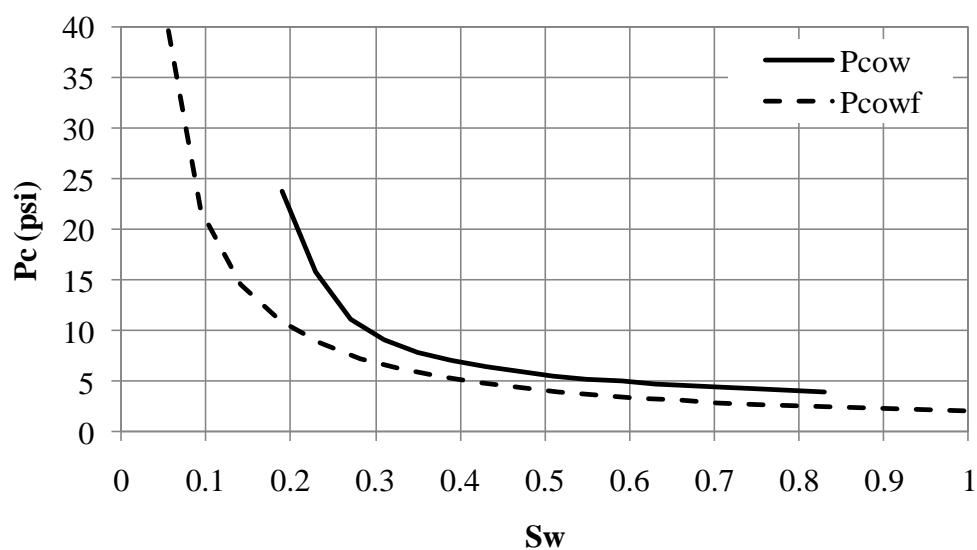
Figure 4-10: Capillary pressure curves on both matrix and fracture obtained from history matching method.

Figure 4-11 shows an independent validation of relative permeability curves obtained from the history matching methods, against experimental measurements using steady-state two-phase displacement in cylindrical cores. The curves obtained from the history match are slightly lower than the experimental ones, which is attributed to the fact that the steady-state displacement experiment took place is a co-current manner, while the history matched results correspond primarily to counter-current flow. The difference in the magnitude of co-current and counter-current relative permeabilities is consistent with findings reported by Bourbiaux and Kalaydjian (1990).
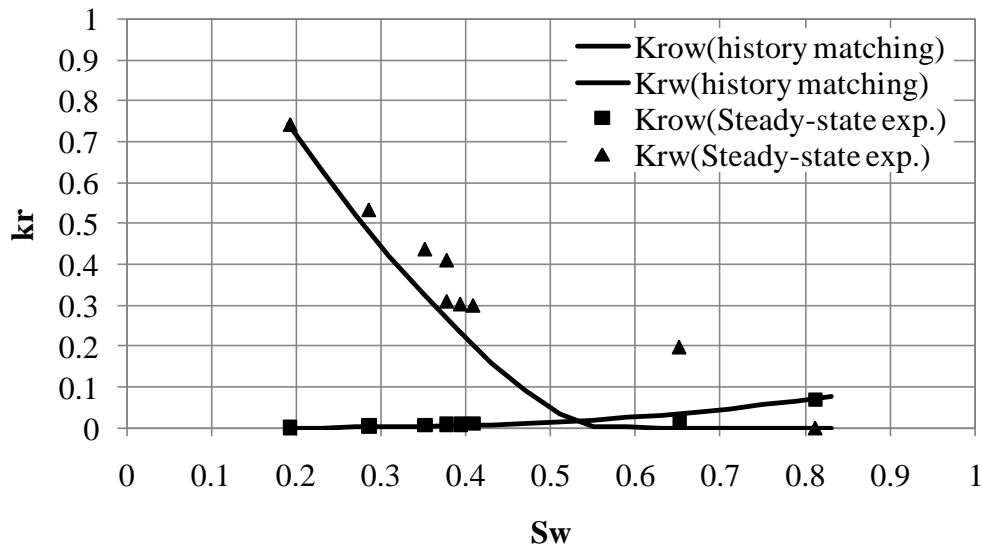
Figure 4-11: Comparison of experimental and history matched relative permeability curves.

A comparison of modeled and experimental saturation changes as a function of time and pore volume injected reveal excellent agreement, as seen in Figure 4-12. A one-on-one comparison of modeled and experimental saturation maps is presented in Figure 4-13, and confirms the goodness of the proposed modeling methodology and the transport properties derived from its implementation. Figure 4-14 also shows good agreement of temporal vertical saturation profiles. The progression of the modeled imbibition front at

early time seems to be slightly ahead of the experimental front in Figure 4-14, which can be explained through small differences in the continuity of the fracture zone and the simplified representation of the fracture by a row of grid blocks having uniform properties.

Figure 4-12: Comparison of experimental and modeled average water saturation as a function of time at 4mL/hr water injection rate.

Experimental results

10min	30min	50min	80min	110min	170min	230min	1430min

Simulation results

10min	30min	50min	80min	110min	170min	230min	1430min

Residual saturations

10min	30min	50min	80min	110min	170min	230min	1430min

Figure 4-13: Comparison of experimental and modeled water saturation maps at 4 mL/hr water injection rate.

Figure 4-14: Comparison of experimental and modeled vertical saturation profiles perpendicular to the fracture and averaged over the central 6 mm of the sample, q=4mL/hr.

An additional test of the validity of the modeled system and transport properties was performed by predicting the evolution of the imbibition front and saturation changes at a higher injection rate, for which we also had experimental data. This data set at higher injection rate was not presented to the model during the history match process, but rather used to assess the accuracy of the predictions. When using the matched transport properties to predict imbibition front evolution at a higher injection rate of 40mL/hr, the prediction still showed excellent agreement as displayed in Figure 4-15 through Figure 4-17.

Simulation results from different injection rates, in Figure 4-12 and Figure 4-15, show that higher-rate curve (q=40mL/hr) reaches higher water saturation, and thus higher oil displacement, at the expense of more pore volumes injected. The rate of injection is also responsible for the shape of the imbibing front, which is farther away from the fracture inlet than the outlet, as shown in Figure 4-16. This observation is less pronounced when the rate of injection is reduced, as shown in Figure 4-13. In addition, for approximately the same pore volume injected, that is 10min (0.36PVI) at high-rate case and 110min (0.33PVI) at low-rate case, we observe a much larger imbibed region in the low-rate case. This implies low injection rate (4mL/hr) allows a more effective spreading of water for the same volume injected.

Further quantitative examination of saturation changes can be obtained from vertical saturation profiles, Figure 4-14 and Figure 4-17. For both simulation results, continuous high water saturation is observed in the center of the sample, where the fracture is located. The most noticeable differences between these two vertical profiles are: (1) the speed at which the water front moves away from the fracture, and (2) the change in saturation as moves away from the fracture. Figure 4-14 shows a gradual saturation change at the front, while there is a relative sharp drop in saturation across the water front in Figure 4-17. Furthermore, water saturations remain in the 0.50-to-0.55 range within the imbibed zone, which is consistent with the previous experimental results.
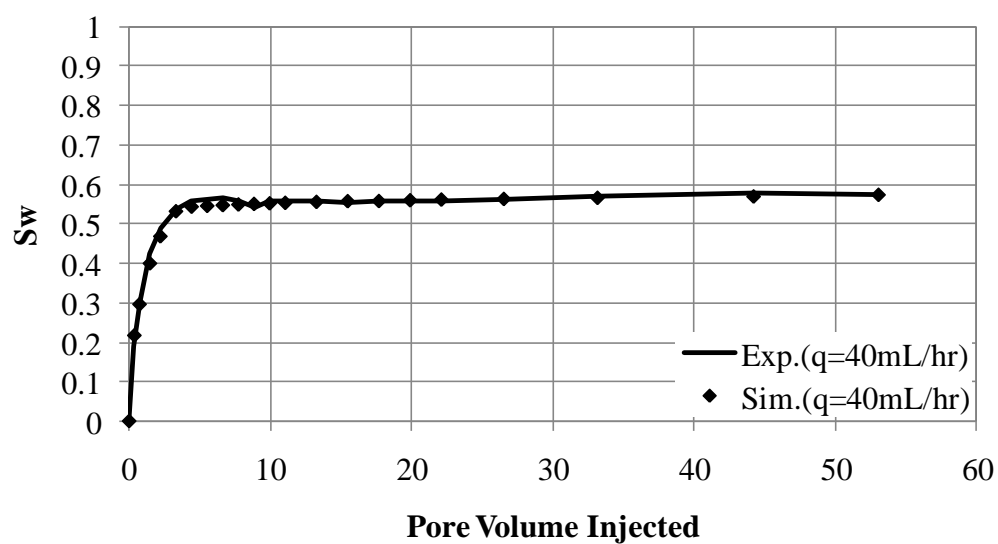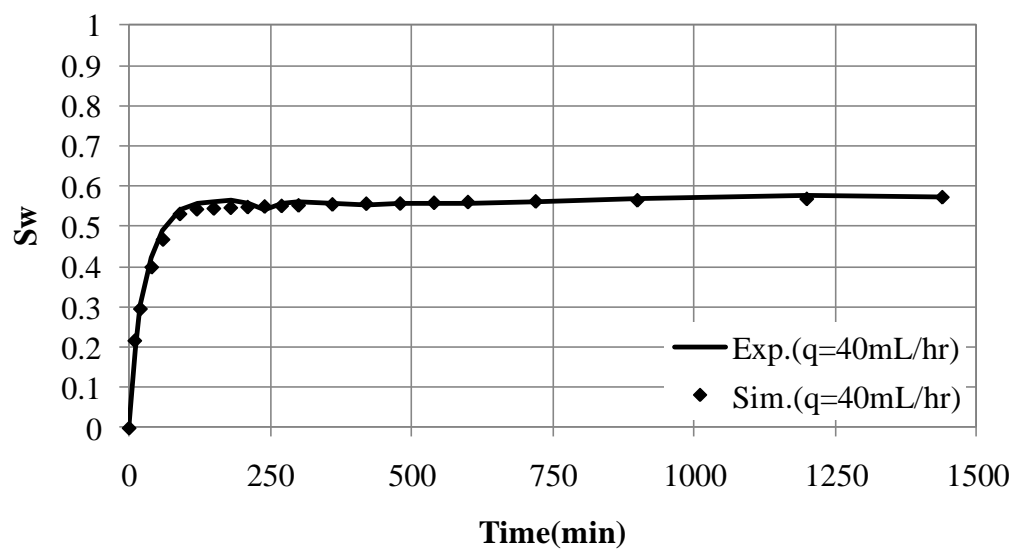
Figure 4-15: Comparison of experimental and predicted average water saturation as a function of time at 40mL/hr water injection rate.
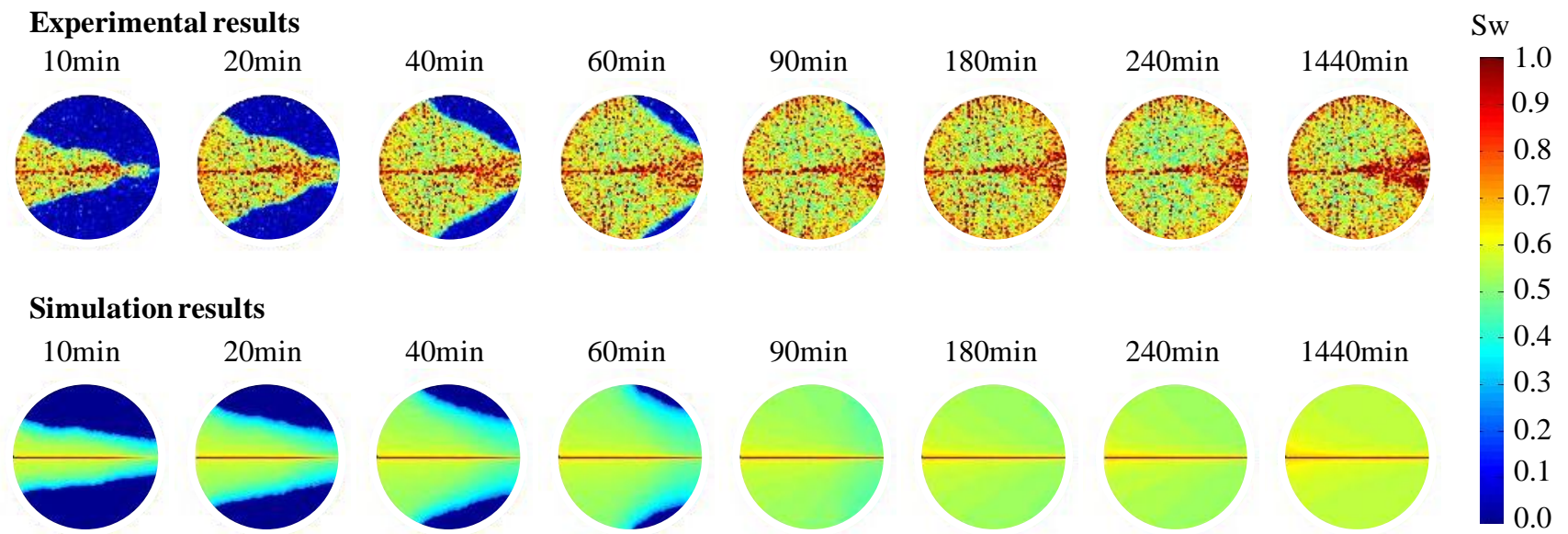
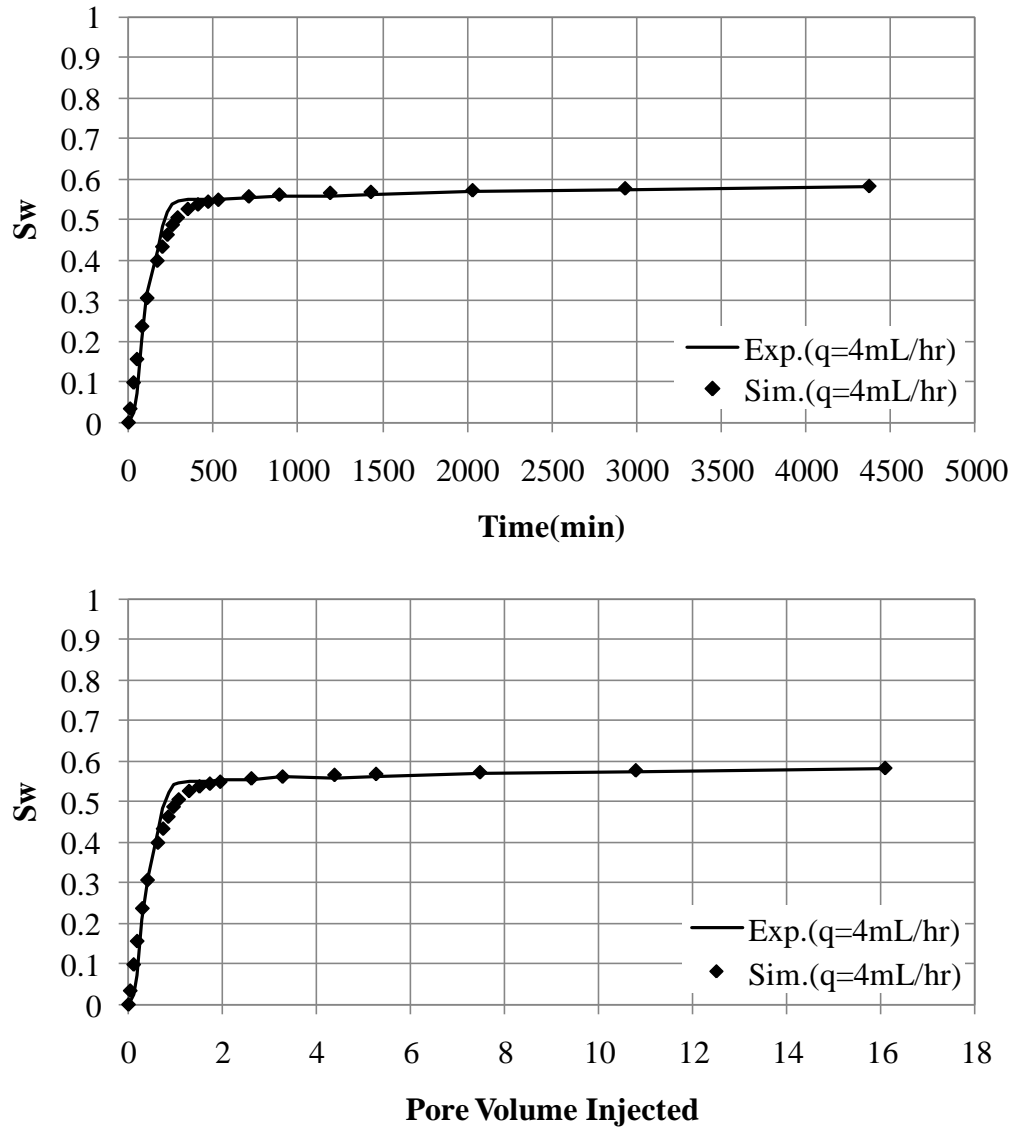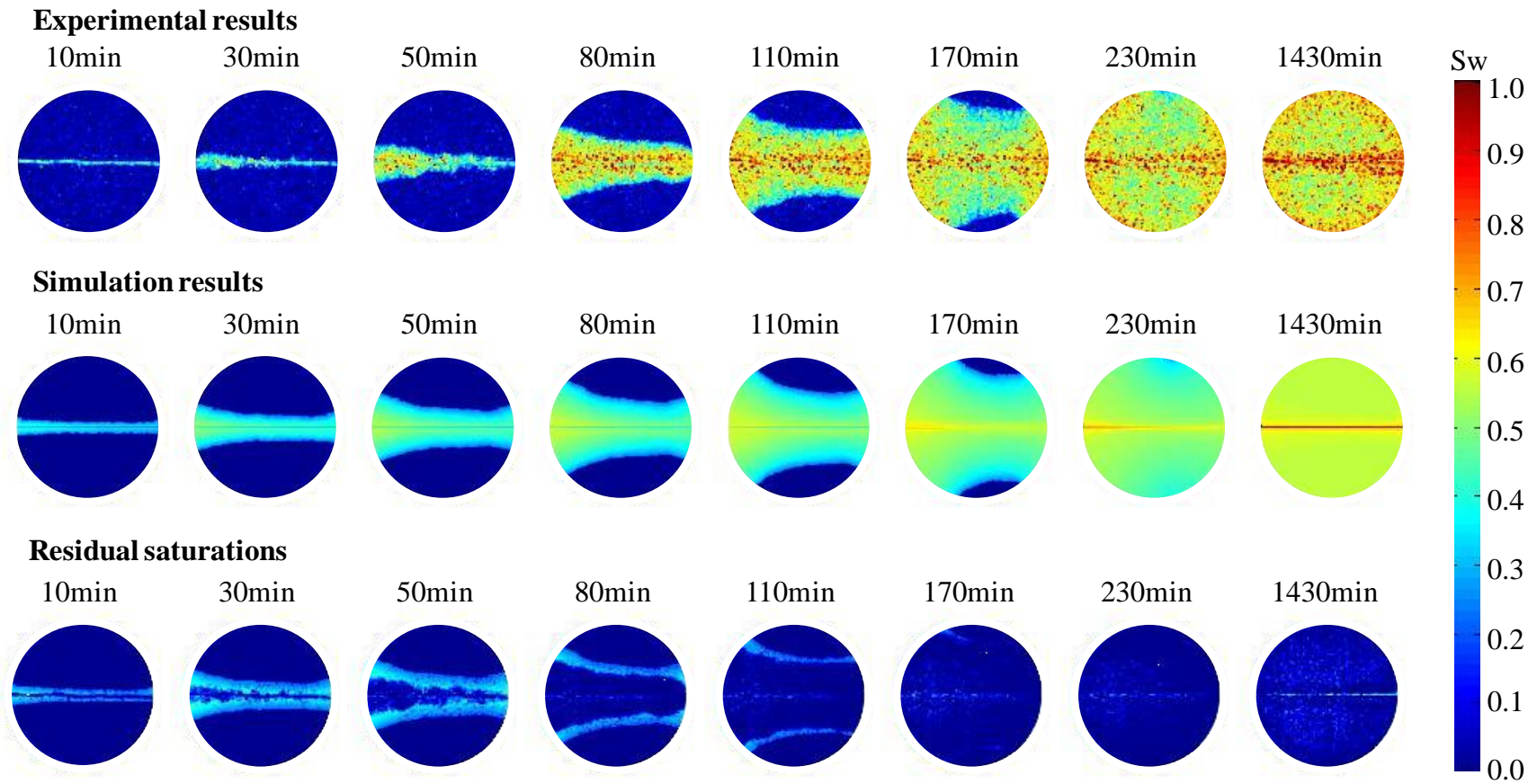Figure 4-16: Comparison of experimental and predicted water saturation maps at 40 mL/hr water injection rate.
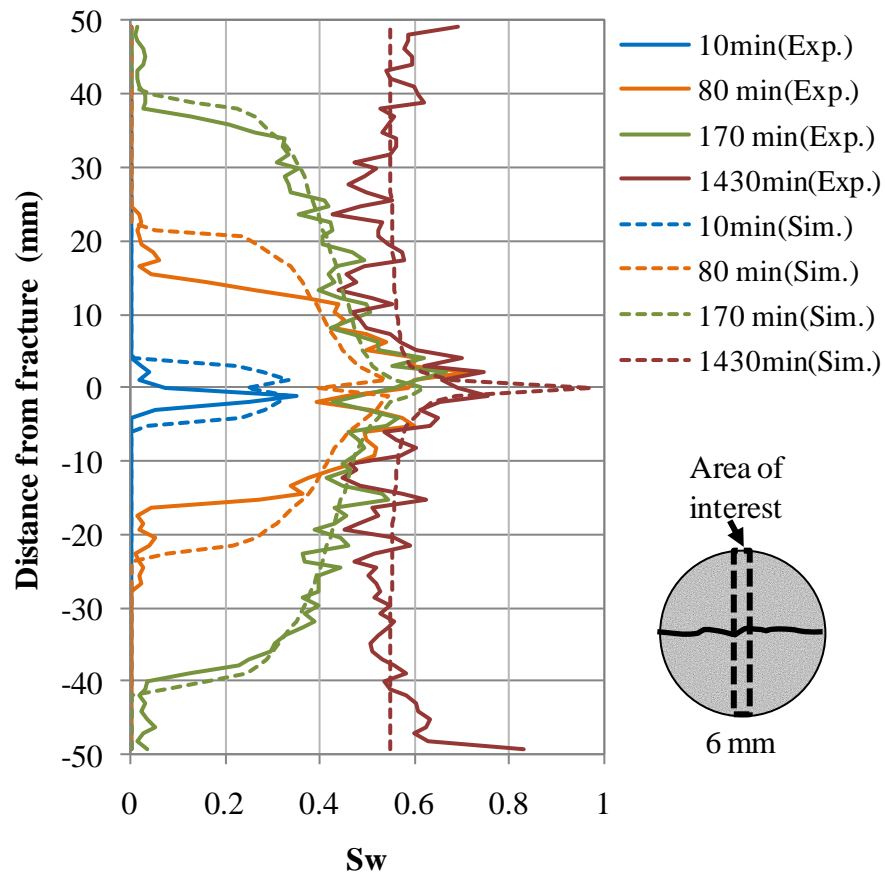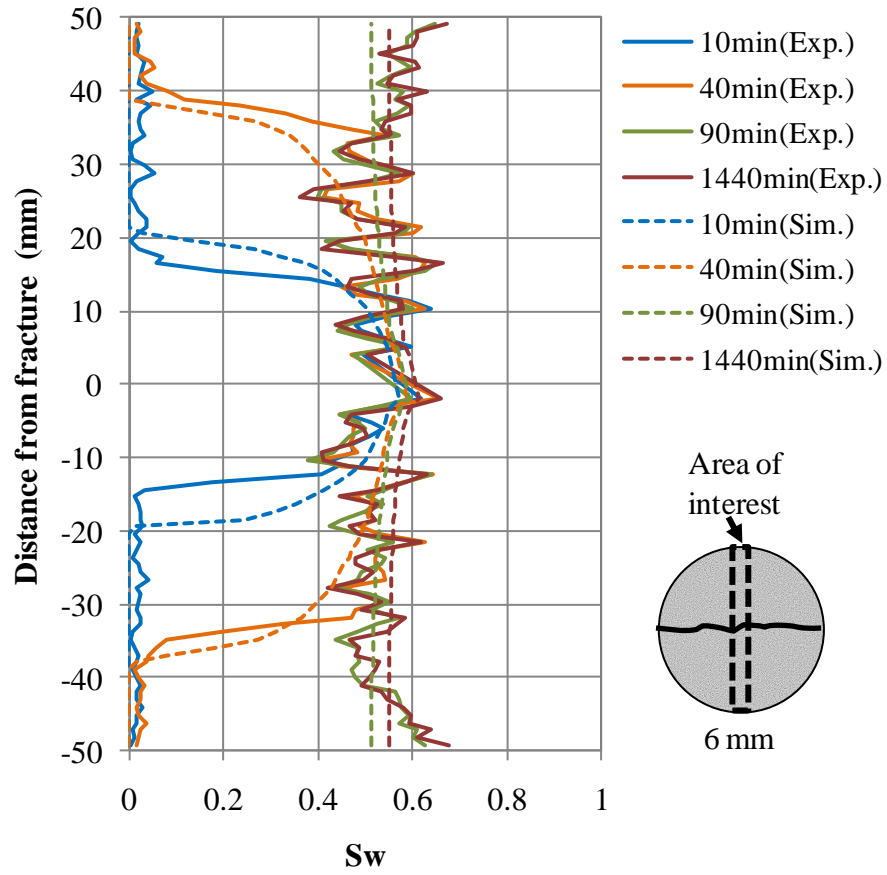
Figure 4-17: Comparison of experimental and predicted vertical saturation profiles perpendicular to the fracture and averaged over the central 6 mm of the sample, q=40mL/hr.

.

4.5 Predictive Cases

Having established a solid level of confidence in the modeled system, relative to its experimental counterpart, allowed us to design additional predictive scenarios to explore the influence of matrix homogeneity/heterogeneity and boundary shape on the response of the imbibition front. To investigate the influence of matrix homogeneity/heterogeneity on water front evolution, we compare three different porosity and permeability distributions as cases A, E and F with the same the transport properties provided in Figure 4-9 and Figure 4-10. This investigation can also help to explain the mismatching of faster water front evolving at early time in Figure 4-14. In circular systems, the water front hits outer boundaries faster in the inlet than the outlet.

Case A: reference case.

The average porosity and permeability are the same in all additional predictive cases. Their standard deviation in porosity and permeability are also listed in Table 4-3.

Case E: as homogeneous systems.

In case E, a single porosity (0.2273) and permeability (76.5 md) value were applied for entire modeled system except the fracture zone. A more uniform porosity and permeability distribution is expected to obtained than that in case A.

Table 4-3: Standard deviation of porosity and permeability for cases A, E, F and G.

Case	Standard deviation of Porosity(mean=0.2273)	Standard deviation of Permeability(mean=76.5mD)
A	0.04	45.02
E	0.00	0.00
F	0.09	169.83
G	0.04	45.02

Case F: as heterogeneous systems,

In case F, matrix porosity variations were increased according to following equation:

$$\phi_{pix\_new} = a \cdot (\phi_{pix} - \phi_{avg}) + \phi_{avg}$$

where a is deviation factor (a=3), ϕ_{avg} and ϕ_{pix} are average and pixel porosity respectively. Timur's correlation (Timur (1968)) was used to obtain an absolute permeability value after a porosity distribution map was created. Figure 4-22 displayed porosity and permeability distributions for predictive case F. Figure 4-18 displays porosity and permeability histograms for cases A and F. Porosity and permeability in both cases shape as normal distribution according to Anderson-Darling Normality test (Anderson and Darling (1951)), while reference case A presents as a more sorted system than case F.

Case G: as square boundaries.

To study the effects of boundary shape on imbibing front inclination, which is away from the fracture inlet than the outlet as shown in Figure 4-13 and Figure 4-16, in case G, we change circular boundary as a square boundary using the same rock and fluid properties of reference case A. This additional case study can help to understand the effects of boundary shape on imbibing front inclination.
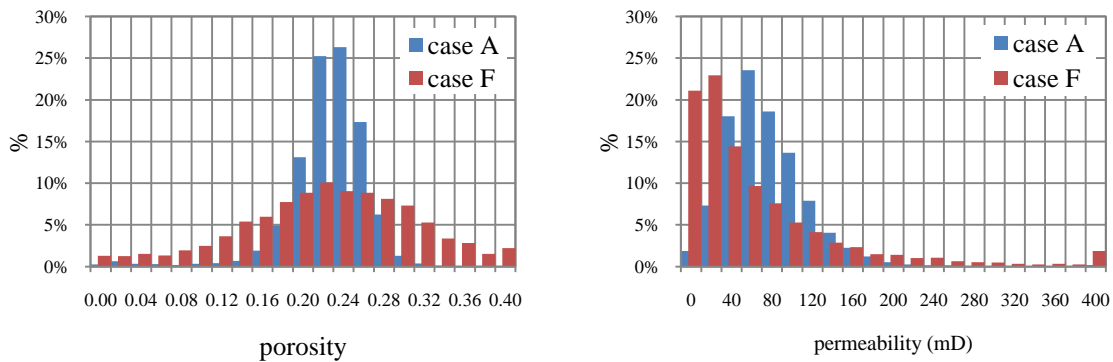
Figure 4-18: Matrix porosity (left) and permeability (right) histograms for cases A and F.

Figure 4-19 presents average saturation changes as a function of time for cases A, E, F and G. The results show oil displacement rate is nearly identical for cases A, E and G throughout the entire simulations. Close examination of case E, the homogeneous system, shows that saturations begin to separate from case A and increase slightly faster after around 100 minutes of water injection. Further increments become negligible after 400 minutes and reach a final water saturation of about 0.56. This can be explained by the fact that rock properties of the reference case A are close to homogeneous. However, in case F (heterogeneous system), saturations separate from case A after 30 minutes injection, and increase at a slower rate with respect to case A. After 1400 minutes of injection, saturation reaches a final saturation value of 0.55. It indicates the increase matrix heterogeneity decreases oil displacement rate. It also confirms the previous observation that the displacement rate is mainly controlled by relative permeabilities. Furthermore, in case G, we change the circular boundaries to square boundaries. Saturation distributions obtained from case G are nearly identical to the reference cases A, implying that the shape of the boundaries has low effect on oil displacement under capillary dominant condition.
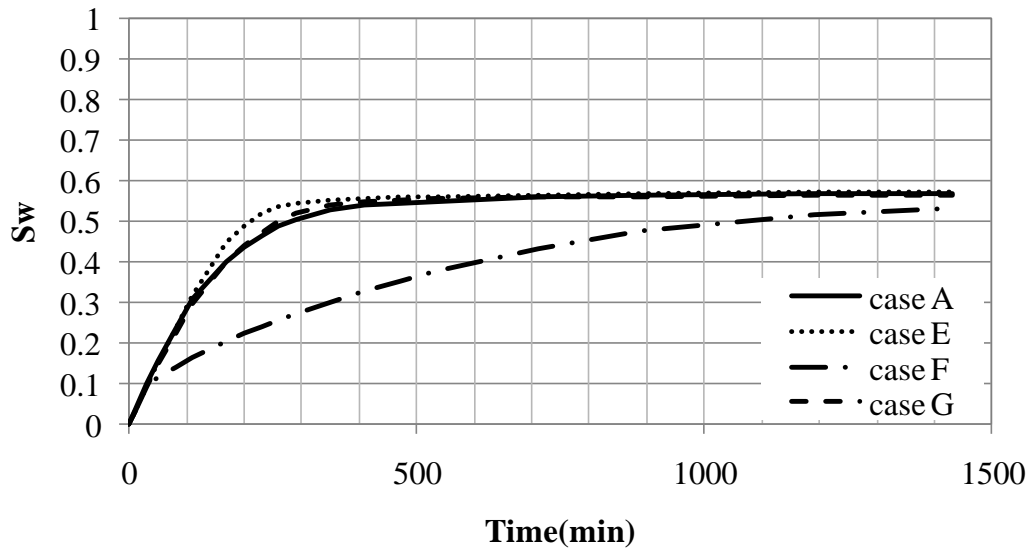
Figure 4-19: Average water saturation as a function of time at 4mL/hr water injection rate for cases A, E, F and G.

Similar observations are made from the time progressions of water saturation maps in Figure 4-20. Case E, the homogeneous system, shows a slightly faster water front extension respect to reference case A, while an unsmooth and slower water front progression was observed in case F, the heterogeneous systems. This result extends our previous conclusions that the reason for the mismatch of water front at early time in Figure 4-14 is not limited to the continuity of the fracture zone and the simplified representation of the fracture. An up-scaling scheme for the simulation model could create a smooth property distribution and a more homogeneous system that can contribute to the speed of water front evolution. In addition, the system with square boundary (case G), shows similar results to the system with circular boundary (case A), confirming that the rate of injection is responsible for the shape of the imbibing front, and this effect is less pronounced when the rate of injection is reducing. Under capillary-dominant counter-current flow regimes, the shape of the boundary has a minimal effect on shape of imbibing front evolution.
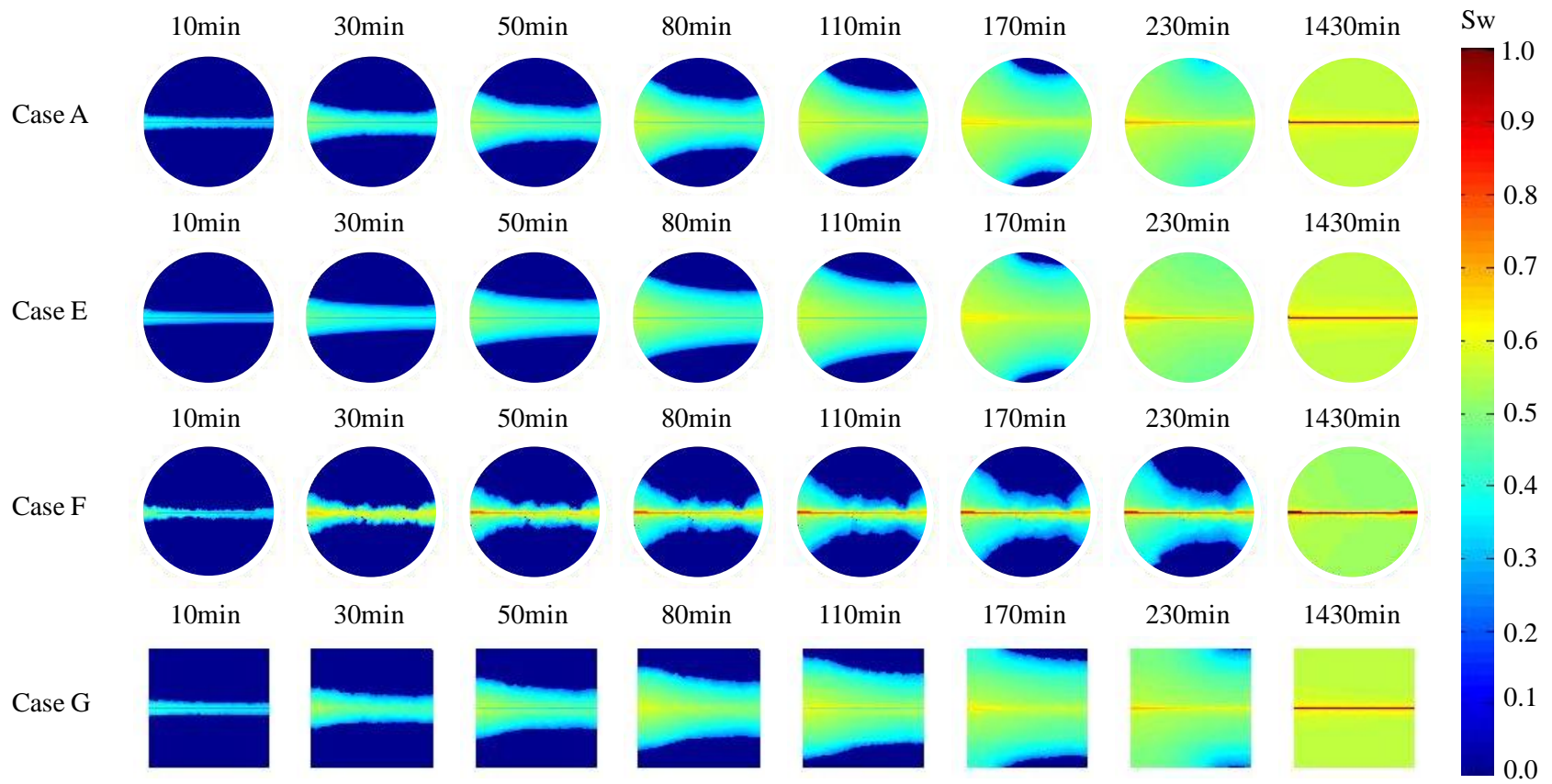
Figure 4-20: Predicted sequence of water saturation maps at 4mL/hr water injection rate for cases A, E, F and G.

Chapter 5

Conclusions

Understanding and predicting the migration of fluids in fractured geologic systems is of great importance in many geological applications, be it for remediation, recovery, storage, or sequestration. In this study, we analyze the impact of injection rate, viscosity ratio, fracture orientation and transport properties on recovery and imbibition front evolution in fractured sandstone, under capillary dominated conditions. Results lead to the following conclusions:

- The higher injection flow rate (q=40mL/hr) shows higher oil recovery, at the expense of more pore volumes injected to reach the ultimate oil recovery. A sharp imbibing front is observed in the high-rate experiment, while a smoother saturation gradient is observed at low rate. Water saturation in the imbibed zone remains constant at around 0.50-to-0.55, suggesting a dynamic equilibrium in the mobility of oil and water phases. We also describe the counter-current flow mechanisms that are evident from the experimental results, and support our observations on the evolution of saturation maps and profiles obtained in the laboratory.

- Co-current flow dominates in the case of water displacing air, while counter-current flow dominates in the case of water displacing kerosene. Liquid-liquid (in the case of water displacing kerosene) and gas-liquid (in the case of water displacing air) imbibition results show significant differences in the shape of the imbibing front, breakthrough time, and saturation profiles. Capillary forces are significantly hindered in the case of water displacing viscous oil when the viscosity of the displaced phase increases, thus making the overall process viscous dominated.

- The influence of fracture orientation on the shape of the imbibing front, and ultimate recovery, was minimal for the time- and length-scales considered in this investigation. However, the varying relevance of gravity at different fracture inclinations still causes changes in water saturation distribution behind the imbibing front, and breakthrough time. Water breakthrough also switches the fracture-matrix transfer mechanism from co-current to counter-current, thus limiting additional recovery of the resident fluid phase. In addition, there is direct evidence of snap-off inside the fracture when the invading front in the matrix moves ahead of the invading front in the fracture.

- Final saturation and ultimate displacement are most sensitive to relative permeability ratio between oil and water phase. Relative permeability to water in the matrix, capillary pressure contrast between matrix and fracture, and degree of rock heterogeneity determine the speed and shape of imbibing front progression. The balance of capillarity and relative permeabilities also has a significant impact on the shape of the invasion front, resulting in periods of co-current and counter-current imbibition. Fracture permeability, and capillary pressure contrast between matrix and fracture dominate occurrence of water breakthrough. The impact of boundary shape on imbibition front evolution was found to be minimal under the evaluated flow conditions, which are dominated by capillary forces.

- Additional experimental and numerical analyses in tight sands and shale are required in the future which would be benefit to evaluate migration and trapping of hydraulic fracturing leak-off under shut-in conditions.

References

Ajose, D., Mohanty, K.K.: Compositional Upscaling in Heterogeneous Reservoirs: Effect of Gravity, Capillary Pressure, and Dispersion. In: SPE Annual Technical Conference and Exhibition, Denver, Colorado, USA, 5-8 October 2003

Al-Wadahi, M., Grader, A.S., Ertekin, T.: An Investigation of Three-Phase Counter-Current Flow Using X-Ray Computerized Tomography and Neuro-Simulation Modeling. In: SPE Annual Technical Conference and Exhibition, Dallas, Texas, USA, 1-4 October 2000

Alajmi, A.F.: The Influence of a Fracture Tip on Two-Phase Flow Displacement Processes. Ph.D. , The Pennsylvania State University (2003)

Alajmi, A.F., Grader, A.S.: Analysis of Fracture-Matrix Fluid Flow Interactions Using X-Ray CT. In: SPE Eastern Meeting, Morgantown, West Virginia, 17-19 October 2000

Anderson, T.W., Darling, D.A.: Asymptotic Theory of Certain Goodness of Fit Criteria Based on Stochastic Processes. Annals of Mathematical Statistics **22**(1), 143-143 (1951)

Angeles, R., Torres-Verdín, C., Hadibeik, A., Sepehrnoori, K.: Estimation of Capillary Pressure and Relative Permeability from Formation-Tester Measurements using Design of Experiment and Data-Weighing Inversion: Synthetic and Field Examples. Journal of Petroleum Science and Engineering (2010). doi:10.1016/j.petrol.2010.10.006

Archer, J.S., Wong, S.W.: Use of a Reservoir Simulator To Interpret Laboratory Waterflood Data SPE Journal **13**(6), 5 (1973)

Babadagli, T.: Injection Rate Controlled Capillary Imbibition Transfer in Fractured Systems. In: SPE Annual Technical Conference and Exhibition, New Orleans, LA, USA, 25-28 September 1994

Babadagli, T.: Efficiency of capillary imbibition dominated displacement of nonwetting phase by wetting phase in fractured porous media. Transport in Porous Media **40**(3), 323-344 (2000)

Basbug, B., Karpyn, Z.T.: Determination of Relative Permeability and Capillary Pressure Curves Using an Automated History-Matching Approach. Paper presented at the SPE Eastern Regional/AAPG Eastern Section Joint Meeting, Pittsburgh, Pennsylvania, USA, 11-15 October 2008

Berkowitz, B.: Characterizing flow and transport in fractured geological media: a review. Advance in Water Resources **25**, 24 (2002)

Bertels, S.P., DiCarlo, D.A., Blunt, M.J.: Measurement of aperture distribution, capillary pressure, relative permeability, and in situ saturation in a rock fracture using computed tomography scanning. Water Resources Research **37**(3), 649-662 (2001)

Bourbiaux, B.J., Kalaydjian, F.J.: Experimental Study of Cocurrent and Countercurrent Flows in Natural Porous Media Spe Reservoir Engineering **5**(3), 361-368 (1990)

Carnes, P.S.: Effects of Natural Fractures or Directional Permeability in Water Flooding. In: SPE Secondary Recovery Symposium, Wichita Falls, Texas, 2-3 May 1966

Chavent, G., Cohen, G., Espy, M.: Determination of Relative Permeability and Capillary Pressure by Automatic Adjustment Method. In: SPE Annual Technical Conference and Exhibition, Dallas, Texas, USA, 21-24 September 1980

Chen, S., Li, G., Peres, A., Reynolds, A.C.: A Well Test for In-Situ Determination of Relative Permeability Curves In: SPE Annual Technical Conference and Exhibition, Dallas, Texas, USA, 9-12 October 2005

Committee on Fracture Characterization and Fluid Flow, N.R.C.: Rock fractures and fluid flow: contemporary understanding and applications. National Academy Press, Washington, D.C. (1996)

Crandall, D., Ahmadi, G., Smith, D.H.: Computational Modeling of Fluid Flow through a Fracture in Permeable Rock. Transport in Porous Media **84**(2), 493-510 (2010). doi:DOI 10.1007/s11242-009-9516-9

Crawford, P.B., Collins, R.E.: Estimated Effect of Vertical Fractures on Secondary Recovery. Transactions of the American Institute of Mining and Metallurgical Engineers **201**, 192-196 (1954)

De la Porte, J.J., Kossack, C.A., Zimmerman, R.W.: The Effect of Fracture Relative Permeabilities and Capillary Pressures on the Numerical Simulation of Naturally Fractured Reservoirs Paper presented at the SPE Annual Technical Conference and Exhibition, Dallas, Texas, USA, 9-12 October 2005

Ding, M., Kantzas, A.: Capillary number correlations for gas-liquid systems. Journal of Canadian Petroleum Technology **46**(2), 27-32 (2007)

Donato, G., Lu, H.Y., Tavassoli, Z., Blunt, M.J.: Multirate-Transfer Dual-Porosity Modeling of Gravity Drainage and Imbibition. SPE Journal **12**(1), 77-88 (2007)

El-Khatib, N.: Development of a Modified Capillary Pressure J-Function In: Middle East Oil Show, Bahrain, 11-14 March 1995

Farzaneh, S.A., Kharrat, R., Ghazanfari, M.H.: Experimental Study of Solvent Flooding to Heavy Oil in Fractured Five-Spot Micro-Models: The Role of Fracture Geometrical Characteristics. Journal of Canadian Petroleum Technology **49**(3), 36-43 (2010)

Firoozabadi, A., Hauge, J.: Capillary-Pressure in Fractured Porous-Media. Journal of Petroleum Technology **42**(6), 784-791 (1990)

Firoozabadi, A., Markeset, T.: An Experimental Study of Capillary and Gravity Crossflow Fractured Porous Media. In: SPE Annual Technical Conference and Exhibition, Washington, DC, 4-7 October 1992

Glass, R.J., Nicholl, M.J., Yarrington, L.: A modified invasion percolation model for low-capillary number immiscible displacements in horizontal rough-walled fractures: Influence of local in-plane curvature. Water Resources Research **34**(12), 3215-3234 (1998)

Gu, Y.G., Yang, C.D.: The Effects of Capillary Force and Gravity on the Interfacial Profile in a Reservoir Fracture or Pore. Journal of Petroleum Science and Engineering **40**(1-2), 77-87 (2003). doi:Doi 10.1016/S0920-4105(03)00104-9

Heaviside, J., Black, C.J.J., Berry, J.F.: Fundamentals of Relative Permeability: Experimental and Theoretical Considerations In: SPE Annual Technical Conference and Exhibition, San Francisco, California, USA, 5-8 October 1983

Hognesen, E.J., Olsen, M., Austad, T.: Capillary and gravity dominated flow regimes in displacement of oil from an oil-wet chalk using cationic surfactant. Energy & Fuels **20**(3), 1118-1122 (2006). doi:Doi 10.1021/Ef050297s

Hoteit, H., Firoozabadi, A.: An efficient numerical model for incompressible two-phase flow in fractured media. Advances in Water Resources **31**(6), 891-905 (2008). doi:DOI 10.1016/j.advwatres.2008.02.004

Ide, S.T., Jessen, K., Orr, F.M., Jr.: Storage of CO2 in saline aquifers: effects of gravity, viscous, and capillary forces on amount and timing of trapping. J. Greenhouse Gas Control **1**, 481-491 (2007)

IMEX: Three-Phase Black Oil Simulator, User's Guide. In. Computer Modeling Group (CMG), Calgary, (2009)

Karpyn, Z.T., Alajmi, A., Radaelli, F., Halleck, P.M., Grader, A.S.: X-ray CT and Hydraulic Evidence for a Relationship between Fracture Conductivity and Adjacent Matrix Porosity. Engineering Geology **103**(3-4), 139-145 (2009). doi:DOI 10.1016/j.enggeo.2008.06.017

Karpyn, Z.T., Li, G., Grader, A.S., Halleck, P.M.: Experimental Conditions Favoring the Formation of Fluid Banks during Counter-Current Flow in Porous Media. Transport in Porous Media **62**(1), 109-124 (2006). doi:DOI 10.1007/s11242-005-0617-9

Keller, A.: High resolution, non-destructive measurement and characterization of fracture apertures. International Journal of Rock Mechanics and Mining Sciences **35**(8), 1037-1050 (1998)

Kruger, W.D.: Determining Areal Permeability Distribution by Calculations Journal of Petroleum Technology **13**(7), 6 (1961)

Lake, L.W.: Enhanced oil recovery. Chapter 3, Prentice Hall Inc., Englewood Cliffs, NJ, USA (1989)

Lee, C.H., Karpyn, Z.T.: Experimental Investigation of Rate Effects on Two-phase Flow through Fractured Rocks Using X-Ray Computed Tomography. Paper presented at the 3rd International Workshop on X-Ray CT for Geomaterials New Orleans, Louisiana, USA, Mar. 1-3

Lefebvre du prey, E.: Gravity and Capillarity Effects on Imbibition in Porous-Media. Society of Petroleum Engineers Journal **18**(3), 195-206 (1978)

Li, G.: History Dependent Modeling of Countercurrent Flow in Porous Media. Ph.D. , The Pennsylvania State University (2003)

Li, K.: A new method for calculating two-phase relative permeability from resistivity data in porous media. Transport in Porous Media **74**(1), 21-33 (2008). doi:DOI 10.1007/s11242-007-9178-4

Li, K., Horne, R.N.: Correlation Between Resistivity Index, Capillary Pressure and Relative Permeability. In: Proceedings World Geothermal Congress 2010, Bali, Indonesia,, 25-29 April 2010

Melean, Y., Broseta, D., Blossey, R.: Imbibition fronts in porous media: effects of initial wetting fluid saturation and flow rate. Journal of Petroleum Science and Engineering **39**(3-4), 327-336 (2003). doi:Doi 10.1016/S0920-4105(03)00072-X

Mohamad Ibrahim, M.N., L.F. Koederitz: Two-Phase Steady-State and Unsteady-State Relative Permeability Prediction Models. In: SPE Middle East Oil Show Bahrain, 17-20 March 2001 2001

Or, D.: Scaling of capillary, gravity and viscous forces affecting flow morphology in unsaturated porous media. Advances in Water Resources **31**(9), 1129-1136 (2008). doi:DOI 10.1016/j.advwatres.2007.10.004

Ovdat, H., Berkowitz, B.: Pore-scale study of drainage displacement under combined capillary and gravity effects in index-matched porous media. Water Resources Research **42**(6), - (2006). doi:Artn W06411 Doi 10.1029/2005wr004553

Pooladi-Darvish, M., Firoozabadi, A.: Cocurrent and countercurrent imbibition in a water-wet matrix block. Spe Journal **5**(1), 3-11 (2000)

Prodanovic, M., Bryant, S.L., Karpyn, Z.T.: Investigating Matrix-Fracture Transfer via a Level Set Method for Drainage and Imbibition. In: SPE Annual Technical Conference and Exhibition, Denver, Colorado, 21-24 September 2008

Rangel-German, E., Akin, S., Castanier, L.: Multiphase-Flow Properties of Fractured Porous Media. Journal of Petroleum Science and Engineering **51**(3-4), 197-213 (2006). doi:DOI 10.1016/j.petrol.2005.12.010

Rangel-German, E.R., Kovscek, A.R.: Experimental and analytical study of multidimensional imbibition in fractured porous media. Journal of Petroleum Science and Engineering **36**(1-2), 45-60 (2002). doi:Pii S0920-4105(02)00250-4

Rangel-German, E.R., Kovscek, A.R.: Matrix-Fracture Shape Factors and Multiphase-Flow Properties of Fractured Porous Media Paper presented at the SPE Latin American and Caribbean Petroleum Engineering Conference, Rio de Janeiro, Brazil, 20-23 June 2005

Rangel-German, E.R., Kovscek, A.R.: A micromodel investigation of two-phase matrix-fracture transfer mechanisms. Water Resources Research **42**(3), 1-13 (2006). doi:Artn W03401 Doi 10.1029/2004wr003918

Shedid, S.A.: Influences of fracture orientation on oil recovery by water and polymer flooding processes: An experimental approach. Journal of Petroleum Science and Engineering **50**(3-4), 285-292 (2006). doi:DOI 10.1016/j.petrol.2005.12.002

Shedid, S.A., Zekri, A.Y.: An experimental approach of influences of perforated length and fractures on horizontal well productivity. Journal of Canadian Petroleum Technology **45**(5), 43-48 (2006)

Tang, G., Firoozabadi, A.: Effect of Viscous Forces and Initial Water Saturation on Water Injection in Water-Wet and Mixed-Wet Fractured Porous Media. In: SPE/DOE Improved Oil Recovery Symposium, Tulsa, Oklahoma, 3-5 April 2000

Tavassoli, Z., Zimmerman, R.W., Blunt, M.J.: Analysis of Counter-current Imbibition with Gravity in Weakly Water-Wet Systems. Journal of Petroleum Science and Engineering **48**(1-2), 94-104 (2005a). doi:DOI 10.1016/j.petrol.2005.04.003

Tavassoli, Z., Zimmerman, R.W., Blunt, M.J.: Analytic Analysis for Oil Recovery during Counter-current Imbibition in Strongly Water-Wet Systems. Transport in Porous Media **58**(1-2), 173-189 (2005b). doi:DOI 10.1007/s11242-004-5474-4

Timur, A.: An Investigation of Permeability, Porosity, and Residual Water Saturation Relationship for Sandstone Reservoirs. Paper presented at the SPWLA 9th Annual Logging Symposium, June 23-26

Vinegar, H.J., Wellington, S.L.: Tomographic Imaging of 3-phase Flow Experiments. Review of Scientific Instruments **58**(1), 96-107 (1987)

Appendix A

Derivative of Porosity and Fluid saturations from CT Scans

A.1 Kerosene-Brine System

1   Average Porosity

$$\phi_{avg} = \frac{V_{oil\_injected}}{V_{Bulk\_volume} - V_{dead\_volume}}$$ ………………..……………...................[1]

2   Pixel Porosity

when pore space was 100% saturated with oil

$$CT_{oil\_sat,pixel} = CT_{matrix} \cdot (1 - \phi_{pixel}) + CT_{oil} \cdot \phi_{pixel}$$ …………………...……….............[2]

$$CT_{oil\_sat,avg} = CT_{matrix} \cdot (1 - \phi_{avg}) + CT_{oil} \cdot \phi_{avg}$$ ……….............……..…..................[3]

during vacuum condition

$$CT_{vacuum,pixel} = CT_{matrix} \cdot (1 - \phi_{pixel}) + CT_{vacuum} \cdot \phi_{pixel}$$ ……………....................[4]

$$CT_{vacuum,avg} = CT_{matrix} \cdot (1 - \phi_{avg}) + CT_{vacuum} \cdot \phi_{avg}$$ …………..............…...............[5]

By subtracting equation [2] and [4], we have

$$CT_{oil\_sat,pixel} - CT_{vacuum,pixel} = (CT_{oil} - CT_{vacuum}) \cdot \phi_{pixel}$$

$$\phi_{pixel} = \frac{CT_{oil\_sat,pixel} - CT_{vacuum,pixel}}{CT_{oil} - CT_{vacuum}}$$ ……………….......................................[6]

By subtracting equation [3] and [5], we have

$$CT_{oil\_sat,avg} - CT_{vacuum,avg} = (CT_{oil} - CT_{vacuum}) \cdot \phi_{avg}$$

$$CT_{oil} - CT_{vacuum} = \frac{CT_{oil\_sat,pixel} - CT_{vacuum,pixel}}{\phi_{avg}}$$ ……....................................[7]

[7] into [6]

$$\phi_{pixel} = \frac{CT_{oil\_sat,pixel} - CT_{vacuum,pixel}}{CT_{oil\_sat,avg} - CT_{vacuum,avg}} \phi_{avg}$$

.....…………………………………...……..........[8]

3   Average water saturation:

$$S_{w,avg} = \frac{CT_{f,avg} - CT_{oil\_sat,avg}}{CT_{water\_sat,avg} - CT_{oil\_sat,avg}}$$

…………….....................…..……………......….......[9]

4   pixel water saturation:

As a co-existence of kerosene and water in the pore space (*f*).

$$CT_{f,pixel} = CT_{matrix} \cdot (1 - \phi_{pixel}) + CT_{oil} \cdot \phi_{pixel} \cdot (1 - S_{w,pixel}) + CT_{water} \cdot \phi_{pixel} \cdot S_{w,pixel}$$

.…….........[10]

$$CT_{f,avg} = CT_{matrix} \cdot (1 - \phi) + CT_{oil} \cdot \phi \cdot (1 - S_w) + CT_{water} \cdot \phi \cdot S_w$$

……..[11]

By subtracting equation [2] and [10], we have

$$CT_{f,pixel} - CT_{oil\_sat,pixel} = CT_{water} \cdot \phi_{pixel} \cdot S_{w,pixel} - CT_{oil} \cdot \phi_{pixel} \cdot S_{w,pixel}$$

$$S_{w,pixel} = \frac{CT_{f,pixel} - CT_{oil\_sat,pixel}}{CT_{water} - CT_{oil}} \cdot \frac{1}{\phi_{pixel}}$$

……...[12]

By subtracting equation [3] and [11], we have

$$CT_{f,avg} - CT_{oil\_sat,avg} = CT_{water} \cdot \phi \cdot S_w - CT_{oil} \cdot \phi \cdot S_w$$

$$CT_{water} - CT_{oil} = \frac{CT_{f,avg} - CT_{oil\_sat,avg}}{\phi_{avg} \cdot S_{w,avg}}$$

……...[13]

[13] into [12]

$$S_{w,pixel} = \frac{CT_{f,pixel} - CT_{oil\_sat,pixel}}{CT_{f,avg} - CT_{oil\_sat,avg}} \cdot \left(\frac{\phi_{avg}}{\phi_{pixel}} \right) \cdot S_{w,avg}$$

………………...….…………….......…………[14]

A.2 Air-Brine System

1   Average Porosity

$$\phi_{avg} = \frac{V_{DW\_injected}}{V_{Bulk\_volume} - V_{dead\_volume}}$$ ………………..………………………...….…...........[1]

2   Pixel Porosity

when pore space was 100% saturated with distilled water

$$CT_{DW\_sat,pixel} = CT_{matrix} \cdot (1-\phi_{pixel}) + CT_{DW} \cdot \phi_{pixel}$$ ………………………………...……..[15]

$$CT_{DW\_sat,avg} = CT_{matrix} \cdot (1-\phi_{avg}) + CT_{DW} \cdot \phi_{avg}$$ ……………………….........…….......[16]

By subtracting equation [15] and [2], we have

$$CT_{DW\_sat,pixel} - CT_{vacuum,pixel} = (CT_{DW} - CT_{vacuum}) \cdot \phi_{pixel}$$

$$\phi_{pixel} = \frac{CT_{DW\_sat,pixel} - CT_{vacuum,pixel}}{CT_{DW} - CT_{vacuum}}$$

… … … … … … . . . .…. . . . . [1 7]

By subtracting equation [16] and [5], we have

$$CT_{DW\_sat,avg} - CT_{vacuum,avg} = (CT_{DW} - CT_{vacuum}) \cdot \phi_{avg}$$

$$CT_{DW} - CT_{vacuum} = \frac{CT_{DW\_sat,avg} - CT_{vacuum,avg}}{\phi_{avg}}$$ ……………......................................[18]

[18] into [17]

$$\phi_{pixel} = \frac{CT_{DW\_sat,pixel} - CT_{vacuum,pixel}}{CT_{DW\_sat,avg} - CT_{vacuum,avg}} \phi_{avg}$$ …………………………………..............[19]

3   Average water saturation:

$$S_{w,avg} = S_{wi,avg} + \Delta S_{w,avg}$$ ……………….....................………….….…......…………….... [20]

3.1   Initial water saturation(with distilled water)

$$S_{wi,avg} = \frac{CT_{initial\_DW,avg} - CT_{vacuum,avg}}{CT_{DW\_sat,avg} - CT_{vacuum,avg}}$$ …………..…………….…………........ [21]

3.2 Water saturation increments(Brine)

$$\Delta S_{w,avg} = \frac{CT_{f,avg} - CT_{initial\_DW,avg}}{CT_{brine\_sat,avg} - CT_{initial\_DW,avg}}$$ ………..……………..............…….…. [22]

4 Pixel water saturation

$$S_{w,pixel} = S_{wi,pixel} + \Delta S_{w,pixel}$$ ………….....………...………………….……….... [23]

4.1 Initial water saturation (distilled water)

when pore space was 100% saturated with air

$$CT_{air\_sat,pixel} = CT_{matrix} \cdot (1 - \phi_{pixel}) + CT_{air} \cdot \phi_{pixel}$$ ....[24]

when there was residual DW in pore space

$$CT_{initial\_DW,pixel} = CT_{matrix} \cdot (1 - \phi_{pixel}) + CT_{air} \cdot \phi_{pixel} \cdot (1 - S_{wi,pixel}) + CT_{DW} \cdot \phi_{pixel} \cdot S_{wi,pixel}$$
....[25]

By subtracting equation [24] and [25]

$$CT_{initial\_DW,pixel} - CT_{air\_sat\_pixel} = (CT_{DW} - CT_{air}) \cdot \phi_{pixel} \cdot S_{wi,pixel}$$

$$S_{wi,pixel} = \frac{CT_{initial\_DW,pixel} - CT_{air\_sat\_pixel}}{CT_{DW} - CT_{air}} \cdot \frac{1}{\phi_{pixel}}$$ ....[26]

Assume $CT_{air} \approx CT_{vacuum}$ and recall equation [18]

$$CT_{DW} - CT_{vacuum} = \frac{CT_{DW\_sat,avg} - CT_{vacuum,avg}}{\phi_{avg}}$$ ....[18]

[18] into [26]

$$S_{wi,pixel} = \frac{CT_{initial\_DW,pixel} - CT_{air\_sat\_pixel}}{CT_{DW\_sat,avg} - CT_{vacuum,avg}} \cdot \frac{\phi_{avg}}{\phi_{pixel}}$$ ....[27]

Assume $CT_{air,avg} \approx CT_{vacuum,avg}$ and recall equation [21]

$$CT_{DW\_sat,avg} - CT_{vacuum,avg} = \frac{CT_{DW\_initial,avg} - CT_{vacuum,avg}}{S_{wi,avg}}$$ …….......................... [21]

[21] into [27]

$$S_{wi,pixel} = \frac{CT_{initial\_DW,pixel} - CT_{air\_sat\_pixel}}{CT_{DW\_initial,avg} - CT_{vacuum,avg}} \cdot \frac{\phi_{avg}}{\phi_{pixel}} \cdot S_{wi,avg}$$ ....[28]

4.2   Water saturation increments (with Brine)

As a co-existence of air and brine in the pore space (*f*).

$$CT_{f,pixel} = CT_{matrix} \cdot (1 - \phi_{pixel}) + CT_{air} \cdot \phi_{pixel} \cdot (1 - S_{wi,pixel} - \Delta S_{w,pixel})$$
$$+ CT_{water} \cdot \phi_{pixel} \cdot S_{wi,pixel} + CT_{brine} \cdot \phi_{pixel} \cdot \Delta S_{w,pixel}$$ ....[29]

when there was residual DW in pore space

$$CT_{initial\_DW,pixel} = CT_{matrix} \cdot (1 - \phi_{pixel}) + CT_{air} \cdot \phi_{pixel} \cdot (1 - S_{wi,pixel}) + CT_{DW} \cdot \phi_{pixel} \cdot S_{wi,pixel}$$
………...[30]

By subtracting equation [29] from [30]

$$CT_{f,pixel} - CT_{initial\_DW,pixel} = (CT_{brine} - CT_{air}) \cdot \phi_{pixel} \cdot \Delta S_{w,pixel}$$

$$\Delta S_{w,pixel} = \frac{CT_{f,pixel} - CT_{initial\_DW,pixel}}{(CT_{brine} - CT_{air}) \cdot \phi_{pixel}}$$ …..[31]

since

$$CT_{brine\_sat,avg} - CT_{vacuum,avg} = (CT_{brine} - CT_{vacuum}) \cdot \phi_{avg}$$ ....[32]

[32] into[31]

$$\Delta S_{w,pixel} = \frac{CT_{f,pixel} - CT_{initial\_DW,pixel}}{CT_{brine\_sat,avg} - CT_{vacuum,avg}} \cdot \frac{\phi_{avg}}{\phi_{pixel}}$$ …..[33]

Appendix B

Matlab Code for Automated History Matching

B.1 Optimization

```
clear all
clc
tic
x0=[2.5 1.4 1 3.5];
LB=[0.01 0.01 -3 -3];
UB=[10 10 10 10];
options = optimset;
options = optimset(options,'Display','iter');
options = optimset(options,'TolFun',0.0001);
options = optimset(options,'TolX',0.00001 );
options = optimset(options,'TolCon',0);
options = optimset(options,'FunValCheck','on');

options = optimset(options,'Diagnostics','on');
options = optimset(options,'DiffMaxChange',0.1);
options = optimset(options,'DiffMinChange',0.001 );
options = optimset(options,'LargeScale','on');
[x,resnorm,residual,exitflag,output,lambda,jacobian] = ...
lsqnonlin(@obj_lee_EXP16,x0,LB,UB,options);
toc
```

B.2 Objective Function

```
function F=obj_lee_EXP16(x)
load
('C:\Users\Chunghao\Documents\MATLAB\EXP16(flowrate=4ml_hr)
\EXP16_por_avg5_centralized.mat')
load
('C:\Users\Chunghao\Documents\MATLAB\EXP16(flowrate=4ml_hr)
\EXP16_Kabs_avg5_centralized.mat')
load
('C:\Users\Chunghao\Documents\MATLAB\EXP16(flowrate=4ml_hr)
\EXP16_null.mat')
EXP16_Kabs_jk=EXP16_Kabs_avg5_centralized;
EXP16_Kabs_jk(49,:)=5000;
Swr=0.19;
Sor=1-0.83;
NSw=17;NSwf=19;
```

```matlab
%NSw and NSwf were the number of saturation points...
%that picked within the interval of Swirr and 1-Sor
Nx=97;Ny=1;Nz=97;%grids in x and y direction
Sw=linspace(Swr,1-Sor,NSw);
Krwiro=0.077;
krw=Krwiro*((Sw-0.19)/(1-0.19-0.17)).^x(2);
Krocw=0.7402;
no=10;
kro1=Krocw*((1-Sw-(1-Sw(no)))/(1-0.19-(1-
Sw(no)))).^(1+2/x(1));
kro2=Krocw*((1-Sw-0.17)/(1-0.19-0.17)).^9;
kro1=kro1+kro2(no);
kro=[kro1(1:(no-1)) kro2(no:17)];
CPc=((19.995*x(2))+62.055)/3;
Pcow=zeros(1,NSw);
for j=1:NSw;
    if ((Sw(j)>Swr)&&(Sw(j)<=1-Sor));
        Pcow(j)=CPc/(((Sw(j)-Swr)/(1-Sor-Swr))^(1/x(1)));
    elseif (Sw(j)==Swr);
        Pcow(j)=(1.5)*(CPc/(((Sw(j+1)-Swr)/(1-Sor-
Swr))^(1/x(1))));
    end
end
Pcow(1)=(1.5)*Pcow(3);
Pcow(NSw)=CPc/(((Sw(NSw)-Swr)/(1-Sor-Swr))^(1/x(1)));
load
('C:\Users\Chunghao\Documents\MATLAB\EXP16(flowrate=4ml_hr)
\Swf.mat')
Sorwf=0;
Soirwf=0;
Swcritf=0;
Swconf=0;
Krocwf=1;
Krwirof=0.5;
krwf=Krwirof*((Swf-Swcritf)/(1-Swcritf-Soirwf)).^1.8;
krof=Krocwf*((1-Swf-Sorwf)/(1-Swconf-Sorwf)).^1.8;
krof(19)=0;
CPcf=((6.2*x(4))+20.67)/3;   %fracture

Pcowf=zeros(1,NSwf);
Pcowf(1)=1.5*CPcf/Swf(2); %fracture
for i=1:NSwf-1;
    Pcowf(i+1)=CPcf/Swf(i+1); %fracture
end

%% Modified from Basar's code
fid= fopen('EXP16_CMG.dat','w');
fprintf(fid,'%s\n','*********************************
***********************************');
```

```
fprintf(fid,'%s\n','** EXP16
**');
fprintf(fid,'%s\n','**********************************
***********************************');
fprintf(fid,'%s\n','**********************************
***********************************');
fprintf(fid,'%s\n','** IMEX
**');
fprintf(fid,'%s\n','** 97x1x97
**');
fprintf(fid,'%s\n','** Kerosene-Brine
**');
fprintf(fid,'%s\n','** q=4ml_hr
**');
fprintf(fid,'%s\n','** Horizontal Fracture
**');
fprintf(fid,'%s\n','** LAB UNIT
**');
fprintf(fid,'%s\n','**********************************
***********************************');

fprintf(fid,'%s\n','RESULTS SIMULATOR IMEX');
fprintf(fid,'%s\n','*TITLE1');
fprintf(fid,'%s\n',' ''EXP16'' ');
fprintf(fid,'%s\n','*TITLE2');
fprintf(fid,'%s\n',' ''Kerosene-Brine'' ');
fprintf(fid,'%s\n','*TITLE3');
fprintf(fid,'%s\n',' ''q=4ml_hr'' ');

fprintf(fid,'%s\n','*WPRN   *GRID *TIME');
fprintf(fid,'%s\n','*WPRN   *WELL *TIME');
fprintf(fid,'%s\n','*WPRN   *SECTOR *TIME');

fprintf(fid,'%s\n','*OUTPRN *WELL *ALL');
fprintf(fid,'%s\n','*OUTPRN *GRID *SO *SW *PRES *OILPOT
*BPP');

fprintf(fid,'%s\n','*WSRF   *GRID  *TIME');
fprintf(fid,'%s\n','*WSRF   *WELL  *TIME');
fprintf(fid,'%s\n','*OUTSRF *WELL *ALL');
fprintf(fid,'%s\n','*OUTSRF *GRID *ALL');
fprintf(fid,'%s\n','**OUTSRF *GRID *SO *SW *PRES *OILPOT
*BPP');
fprintf(fid,'%s\n','*OUTSRF *RES *ALL');

fprintf(fid,'%s\n','*INUNIT *LAB');
fprintf(fid,'%s\n','**********************************
***********************************');
fprintf(fid,'%s\n','**SECTION: RESERVOIR DESCRIPTION:
**');
```

```matlab
fprintf(fid,'%s\n','*******************************************************************');

fprintf(fid,'%s %d %d %d\n','*GRID *VARI',Nx,Ny,Nz);
fprintf(fid,'%s\n','*KDIR  *DOWN');

fprintf(fid,'%s\n','*DI    *CON  0.102539063 ** cm');
fprintf(fid,'%s\n','*DJ    *CON  1.0         ** cm');
fprintf(fid,'%s\n','*DK    *CON  0.102539063 ** cm');
fprintf(fid,'%s\n','*DEPTH 1 1 1 -4.921875');
fprintf(fid,'%s\n','*null  *ALL');
for i=1:97;
    for k=1:97;
        fprintf(fid,'%f ',EXP16_null(i,k));
        fprintf(fid,'\n');
    end
end
fprintf(fid,'%s\n','*POR   *ALL');
for i=1:97;
    for k=1:97;
        fprintf(fid,'%f ',EXP16_por_avg5_centralized(i,k));
        fprintf(fid,'\n');
    end
end
fprintf(fid,'%s\n','*PERMI   *ALL');
for i=1:97;
    for k=1:97;
        fprintf(fid,'%f
',EXP16_Kabs_avg5_centralized(i,k));
        fprintf(fid,'\n');
    end
end
fprintf(fid,'%s\n','*PERMJ *ALL');
for i=1:97;
    for k=1:97;
        fprintf(fid,'%f ',EXP16_Kabs_jk(i,k));
        fprintf(fid,'\n');
    end
end
fprintf(fid,'%s\n','*PERMK *ALL');
for i=1:97;
    for k=1:97;
        fprintf(fid,'%f ',EXP16_Kabs_jk(i,k));
        fprintf(fid,'\n');
    end
end
fprintf(fid,'%s\n','*CPOR  *MATRIX 1E-6');
fprintf(fid,'%s\n','*PRPOR *MATRIX 101.325   ** kPa');
fprintf(fid,'%s\n','*MODEL *OILWATER');
```

```
fprintf(fid,'%s\n','********************************
******************************');
fprintf(fid,'%s\n','**SECTION: PVT DATA:
**');
fprintf(fid,'%s\n','********************************
******************************');
fprintf(fid,'%s\n','*PVT *BG 1');

fprintf(fid,'%s\n','**p(kPa)  rs       bo      Bg
viso(mPa-s) visg(mPa-s)');
fprintf(fid,'%s\n','82.9688 1.4768  1.00936 1.25955
2.32164   0.0095245');
fprintf(fid,'%s\n','124.26  1.76531 1.01002 0.839518
2.29698   0.0095319');
fprintf(fid,'%s\n','165.552 2.0621  1.0107  0.629009
2.27224   0.00953988');
fprintf(fid,'%s\n','206.843 2.36635 1.01139 0.502545
2.24752   0.00954833');
fprintf(fid,'%s\n','240.077 2.6162  1.01196 0.432355
2.22769   0.00955543');
fprintf(fid,'%s\n','300 3.07697 1.01303 0.345095  2.19219
0.00956883');

fprintf(fid,'%s\n','*DENSITY *OIL      0.8136 ** g/cm3');
fprintf(fid,'%s\n','*DENSITY *GAS      0.0012 ** g/cm3');
fprintf(fid,'%s\n','*DENSITY *WATER    1.1456 ** g/cm3');

fprintf(fid,'%s\n','*CO         0.000896311');
fprintf(fid,'%s\n','*BWI        1.00000 ');
fprintf(fid,'%s\n','*CW         0');
fprintf(fid,'%s\n','*REFPW    101.325');
fprintf(fid,'%s\n','*VWI        1          ** mPa-s');
fprintf(fid,'%s\n','*CVW        0.0');

fprintf(fid,'%s\n','*ROCKFLUID');
fprintf(fid,'%s\n','********************************
******************************');
fprintf(fid,'%s\n','** Rock-Fluid Property Section
**');
fprintf(fid,'%s\n','********************************
******************************');
fprintf(fid,'%s\n','*RPT 1 *IMBIBITION *PCOW');
fprintf(fid,'%s\n','*EPSPC  0.05');
fprintf(fid,'%s\n','*SWT');
fprintf(fid,'%s\n','** sw krw krow Pcow '); %
for i=1:NSw
    fprintf(fid,'%f %f %f %f\n', Sw(i), krw(i), kro(i),
Pcow(i));
end
```

```
fprintf(fid,'%s\n','*RPT 2 **IMBIBITION **PCOW');
fprintf(fid,'%s\n','*SWT');
fprintf(fid,'%s\n','**   sw   krw     krow     Pcow ');
for i=1:NSwf
  fprintf(fid,'%f %f %f %f\n', Swf(i), krwf(i), (krof(i)),
Pcowf(i));
end

fprintf(fid,'%s\n','*RTYPE *MATRIX   *CON 1');
fprintf(fid,'%s\n','*MOD');
fprintf(fid,'%s\n','1:97 1:1 49:49 = 2');
fprintf(fid,'%s\n','*INITIAL');
fprintf(fid,'%s\n','**************************************
***********************************');
fprintf(fid,'%s\n','** Initial Conditions **');
fprintf(fid,'%s\n','**************************************
***********************************');
fprintf(fid,'%s\n','*USER_INPUT');
fprintf(fid,'%s\n','*PRES *KVAR'); %pressure gradient in Z
direction
fprintf(fid,'%s\n','4*101.3244','8*101.3245','8*101.3246','
8*101.3247','9*101.3248','8*101.3249','8*101.325','8*101.32
51',...

'9*101.3252','8*101.3253','8*101.3254','8*101.3255','3*101.
3256');
fprintf(fid,'%s\n','*PB   *MATRIX *CON 0.386'); %Bubble
point pressure
fprintf(fid,'%s\n','*SO   *MATRIX *CON 1');
fprintf(fid,'%s\n','*DATUMDEPTH 0 *INITIAL');

fprintf(fid,'%s\n','*NUMERICAL');
fprintf(fid,'%s\n','**************************************
***********************************');
fprintf(fid,'%s\n','** Numerical Control Section
**');
fprintf(fid,'%s\n','**************************************
***********************************');
fprintf(fid,'%s\n','*MAXSTEPS  10000000');
fprintf(fid,'%s\n','*AIM  *OFF');
fprintf(fid,'%s\n','*NORM *PRESS 3000.0');  %default value
fprintf(fid,'%s\n','*NORM *SATUR 0.1');     %default value

fprintf(fid,'%s\n','*RUN');
fprintf(fid,'%s\n','*DATE 2010 10 25');
fprintf(fid,'%s\n','**************************************
***********************************');
fprintf(fid,'%s\n','** Well and Recurrent Data Section
**');
```

```
fprintf(fid,'%s\n','********************************
************************************');

fprintf(fid,'%s\n','*DTMAX  0.1   ** minutes');
%fprintf(fid,'%s\n','*DTWELL 0.001 ** minutes');
fprintf(fid,'%s\n','*DTMIN 0.0001 ** minutes');
fprintf(fid,'%s\n','*AIMSET *MATRIX  *CON 1  ** Set all
blocks implicit');

fprintf(fid,'%s %d %s %d
%s\n','*WELL',1,'''PRODUCER',1,'''');
fprintf(fid,'%s %d\n','*PRODUCER',1);
%fprintf(fid,'%s %f %s\n','*OPERATE *MAX *STL',4/60,'**
cm3/min =  m3/D');
fprintf(fid,'%s %f %s\n','*OPERATE *MIN *BHP' ,101.325,'
**kpa');
fprintf(fid,'%s\n','**                     RW,   CC,   WF,
SS');
fprintf(fid,'%s\n','*GEOMETRY  *K      0.01  0.34   1.0
0.0');
fprintf(fid,'%s %d\n','*PERF *GEO',1);
fprintf(fid,'%s\n','** i  j  k  ff');
fprintf(fid,'%d %d %d %s\n',97,1,49, '1.0');

fprintf(fid,'%s %d %s %d %s\n','*WELL',2,
'''INJECTOR',2,'''');
fprintf(fid,'%s %d\n','*INJECTOR *MOBWEIGHT',2);
fprintf(fid,'%s\n','*INCOMP  *WATER');
fprintf(fid,'%s %f %s\n','*OPERATE *MAX *STW',4/60,'**
cm3/min =  m3/D');
fprintf(fid,'%s\n','**                     RW,   CC,   WF,
SS');
fprintf(fid,'%s\n','*GEOMETRY  *K      0.01  0.34   1.0
0.0');
fprintf(fid,'%s %d\n','*PERF *GEO',2);
fprintf(fid,'%s\n','** i  j  k  ff');
fprintf(fid,'%d %d %d %s\n',1,1,49,'1.0');
fprintf(fid,'\n');
fprintf(fid,'%s\n','*TIME 10');
fprintf(fid,'%s\n','*TIME 30');
fprintf(fid,'%s\n','*TIME 50');
fprintf(fid,'%s\n','*TIME 80');
fprintf(fid,'%s\n','*TIME 110');
fprintf(fid,'%s\n','*TIME 170');
fprintf(fid,'%s\n','*TIME 200');
fprintf(fid,'%s\n','*TIME 230');
fprintf(fid,'%s\n','*TIME 260');
fprintf(fid,'%s\n','*TIME 290');
fprintf(fid,'%s\n','*TIME 350');
fprintf(fid,'%s\n','*TIME 410');
```

```
fprintf(fid,'%s\n','*TIME 470');
fprintf(fid,'%s\n','*TIME 530');
fprintf(fid,'%s\n','*TIME 710');
fprintf(fid,'%s\n','*TIME 890');
fprintf(fid,'%s\n','*TIME 1190');
fprintf(fid,'%s\n','*TIME 1430');
fprintf(fid,'%s\n','*TIME 2030');
fprintf(fid,'%s\n','*TIME 2930');
fprintf(fid,'%s\n','*TIME 4370');
fprintf(fid,'%s\n','*STOP');
status=fclose('all');
%%
dos('run_cmg_imex_exe.bat');
dos('run_cmg_report_exe.bat');
%
Sw_read=fopen('SW.INC','r');
reading=fscanf(Sw_read,'%s',1);
i=1;
Sw_map=zeros(97,97);
while(1)
    if strcmp(reading,'J')==1
        reading=fscanf(Sw_read,'%s',1);
        if strcmp(reading,'=')==1
            reading=fscanf(Sw_read,'%s',1);
            if strcmp(reading,'1')==1
                Sw_map(i,:)=fscanf(Sw_read,'%f',[1,97]);
                i=i+1;
            end
        end
    end
    if feof(Sw_read)==1
        break
    end
    reading=fscanf(Sw_read,'%s',1);
end
%%
load
('C:\Users\Chunghao\Documents\MATLAB\EXP16(flowrate=4ml_hr)
\EXP16_97_10.mat')
load
('C:\Users\Chunghao\Documents\MATLAB\EXP16(flowrate=4ml_hr)
\EXP16_97_30.mat')
load
('C:\Users\Chunghao\Documents\MATLAB\EXP16(flowrate=4ml_hr)
\EXP16_97_50.mat')
load
('C:\Users\Chunghao\Documents\MATLAB\EXP16(flowrate=4ml_hr)
\EXP16_97_80.mat')
```

```
load
('C:\Users\Chunghao\Documents\MATLAB\EXP16(flowrate=4ml_hr)
\EXP16_97_110.mat')
load
('C:\Users\Chunghao\Documents\MATLAB\EXP16(flowrate=4ml_hr)
\EXP16_97_170.mat')
load
('C:\Users\Chunghao\Documents\MATLAB\EXP16(flowrate=4ml_hr)
\EXP16_97_200.mat')
load
('C:\Users\Chunghao\Documents\MATLAB\EXP16(flowrate=4ml_hr)
\EXP16_97_230.mat')
load
('C:\Users\Chunghao\Documents\MATLAB\EXP16(flowrate=4ml_hr)
\EXP16_97_260.mat')
load
('C:\Users\Chunghao\Documents\MATLAB\EXP16(flowrate=4ml_hr)
\EXP16_97_290.mat')
load
('C:\Users\Chunghao\Documents\MATLAB\EXP16(flowrate=4ml_hr)
\EXP16_97_350.mat')
load
('C:\Users\Chunghao\Documents\MATLAB\EXP16(flowrate=4ml_hr)
\EXP16_97_410.mat')
load
('C:\Users\Chunghao\Documents\MATLAB\EXP16(flowrate=4ml_hr)
\EXP16_97_470.mat')
load
('C:\Users\Chunghao\Documents\MATLAB\EXP16(flowrate=4ml_hr)
\EXP16_97_530.mat')
load
('C:\Users\Chunghao\Documents\MATLAB\EXP16(flowrate=4ml_hr)
\EXP16_97_710.mat')
load
('C:\Users\Chunghao\Documents\MATLAB\EXP16(flowrate=4ml_hr)
\EXP16_97_890.mat')
load
('C:\Users\Chunghao\Documents\MATLAB\EXP16(flowrate=4ml_hr)
\EXP16_97_1190.mat')
load
('C:\Users\Chunghao\Documents\MATLAB\EXP16(flowrate=4ml_hr)
\EXP16_97_1430.mat')
load
('C:\Users\Chunghao\Documents\MATLAB\EXP16(flowrate=4ml_hr)
\EXP16_97_2030.mat')
load
('C:\Users\Chunghao\Documents\MATLAB\EXP16(flowrate=4ml_hr)
\EXP16_97_2930.mat')
```

```
load
('C:\Users\Chunghao\Documents\MATLAB\EXP16(flowrate=4ml_hr)
\EXP16_97_4370.mat')

EXP16_EXP=cat(1,EXP16_97_10,EXP16_97_30,EXP16_97_50,EXP16_9
7_80,EXP16_97_110,EXP16_97_170,EXP16_97_200,EXP16_97_230,EX
P16_97_260,EXP16_97_290,EXP16_97_350,EXP16_97_410,EXP16_97_
470,EXP16_97_530,EXP16_97_710,EXP16_97_890,EXP16_97_1190,EX
P16_97_1430,EXP16_97_2030,EXP16_97_2930,EXP16_97_4370);

%
EXP16_CMG=Sw_map(1:end,:);

n_Sw_avg=length(EXP16_EXP)/97;
EXP16_CMG_avg=zeros(1,n_Sw_avg);
EXP16_EXP_avg=zeros(1,n_Sw_avg);
EXP16_EXP_profile=zeros(97,n_Sw_avg);
EXP16_CMG_profile=zeros(97,n_Sw_avg);
for i=0:n_Sw_avg-1

EXP16_CMG_avg(1,i+1)=Sw_avg(EXP16_CMG(i*97+1:i*97+97,:),EXP
16_null,97);
EXP16_EXP_avg(1,i+1)=Sw_avg(EXP16_EXP(i*97+1:i*97+97,:),EXP
16_null,97);
EXP16_EXP_profile(1:97,i+1)=mean(EXP16_EXP(i*97+1:i*97+97,4
6:52),2);
EXP16_CMG_profile(1:97,i+1)=mean(EXP16_CMG(i*97+1:i*97+97,4
6:52),2);
end

Time_Line=[0 10 30 50 80 110 170 200 230 260 290 350 410
470 530 710 890 1190 1430 2030 2930 4370];

figure,plot(Time_Line,[0,EXP16_CMG_avg],'-*'...
    ,Time_Line,[0,EXP16_EXP_avg],'-o');
%
height=(0.102539063)*10*linspace(-48,48,97);
figure;
for i=1:6
plot(EXP16_EXP_profile(:,i),height,'b-');hold on;
plot(EXP16_CMG_profile(:,i),height,'r-.');
axis([0 1 -50
50]);xlabel('Sw(fraction)'),ylabel('Height(mm)');
hold on;
end
plot(EXP16_EXP_profile(:,end),height,'b-');
plot(EXP16_CMG_profile(:,end),height,'r-.');
F=(EXP16_CMG_avg-EXP16_EXP_avg)*100;
save residual.mat F
save x0 x
```

VITA

Chung-Hao Lee

Chung-Hao Lee was born in Taipei, Taiwan, in 1976. He received a bachelor's in Resource Engineering from National Cheng Kung University, Taiwan in1999. He pursued his graduate study in the same university and earned a Master's degree in 2001. Between 1999 and 2001 he also worked for Heisei Corporation as an environmental engineer. After he graduated, he served as engineering officer, 2nd lieutenant in Matsu Defense Command, Chinese Army. In 2003, he finished his obligatory military service and joined Energy and Environment Research Laboratories, Industrial Technology Research Institute, Taiwan as an associate researcher. During this period, he was actively involved in several large-scale geological evaluation projects including spent nuclear waste repository, geothermal, and environmental remediation. In August 2007, he started working on his doctoral degree in Petroleum and Natural Gas Engineering at The Pennsylvania State University. He was awarded , 2nd place in the 2010 SPE regional student paper contest for Mid Continent/Rocky Mountain/Eastern region [PhD division]. He is special interested in multiphase flow in porous and fracture media and numerical reservoir simulation. His research works have been published in the conference proceedings and technical journals. He is a member of Society of Petroleum Engineers.